AGU PUBLICATIONS

JGR

Journal of Geophysical Research: Planets

RESEARCH ARTICLE
10.1002/2015JE004863

This article is a companion to *Pan et al.* [2015] doi:10.1002/2015JE004881.

Key Points:
- Sedimentary rock thermal emission model accuracies are within ~15%
- Detrital grains accurately modeled within ~11%
- Matrix phase identification is inconsistent across techniques

Correspondence to:
M. T. Thorpe,
michael.thorpe@stonybrook.edu

Citation:
Thorpe, M. T., A. D. Rogers, T. F. Bristow, and C. Pan (2015), Quantitative compositional analysis of sedimentary materials using thermal emission spectroscopy: 1. Application to sedimentary rocks, *J. Geophys. Res. Planets*, *120*, 1956–1983, doi:10.1002/2015JE004863.

Received 3 JUN 2015
Accepted 28 SEP 2015
Accepted article online 30 SEP 2015
Published online 26 NOV 2015

Quantitative compositional analysis of sedimentary materials using thermal emission spectroscopy: 1. Application to sedimentary rocks

Michael T. Thorpe[1], A. Deanne Rogers[1], Thomas F. Bristow[2], and Cong Pan[1]

[1]Department of Geosciences, State University of New York at Stony Brook, Stony Brook, New York, USA, [2]NASA Ames Research Center, Moffett Field, California, USA

Abstract Thermal emission spectroscopy is used to determine the mineralogy of sandstone and mudstone rocks as part of an investigation of linear spectral mixing between sedimentary constituent phases. With widespread occurrences of sedimentary rocks on the surface of Mars, critical examination of the accuracy associated with quantitative models of mineral abundances derived from thermal emission spectra of sedimentary materials is necessary. Although thermal emission spectroscopy has been previously proven to be a viable technique to obtain quantitative mineralogy from igneous and metamorphic materials, sedimentary rocks, with natural variation of composition, compaction, and grain size, have yet to be examined. In this work, we present an analysis of the thermal emission spectral (~270–1650 cm^{-1}) characteristics of a suite of 13 sandstones and 14 mudstones. X-ray diffraction and traditional point counting procedures were all evaluated in comparison with thermal emission spectroscopy. Results from this work are consistent with previous thermal emission spectroscopy studies and indicate that bulk rock mineral abundances can be estimated within 11.2% for detrital grains (i.e., quartz and feldspars) and 14.8% for all other mineral phases present in both sandstones and mudstones, in comparison to common in situ techniques used for determining bulk rock composition. Clay-sized to fine silt-sized grained phase identification is less accurate, with differences from the known ranging from ~5 to 24% on average. Nevertheless, linear least squares modeling of thermal emission spectra is an advantageous technique for determining abundances of detrital grains and sedimentary matrix and for providing a rapid classification of clastic rocks.

1. Introduction

Early exploration of Mars resulted in a perception of a lunar-like landscape, dominated by volcanic and impact processes [e.g., *Kieffer and Zent*, 1992]. However, with increasing spatial resolving power of subsequent imagers, beginning with Mars Global Surveyor, finely layered outcrops were discovered across many locations, suggesting a rich sedimentary history and possibly aqueous activity [*Malin and Edgett*, 2000]. Since then, geomorphological features consistent with alluvial fans [e.g., *Howard et al.*, 2005; *Irwin et al.*, 2005], deltas [e.g., *Moore et al.*, 2003; *Fassett and Head*, 2005], and sublacustrine slides [e.g., *Metz et al.*, 2009; *Michalski et al.*, 2013] have also been discovered, providing further insight into fluvial and lacustrine processes on the surface of Mars.

Similarly, from global compositional mapping using infrared spectrometers, the surface of Mars is clearly dominated by basaltic compositions [*Bandfield et al.*, 2000]. Rare but large areas of crystalline hematite were discovered, however, providing clear evidence of aqueous mineralization in some regions (one of which was later investigated by the Opportunity rover) [*Christensen et al.*, 2001; *Glotch and Christensen*, 2005; *Glotch and Rogers*, 2007]. Later, with the advent of spectrometers with higher spatial resolution, hundreds of outcrops of sulfate-, carbonate-, chloride-, opaline silica-, and phyllosilicate-bearing units have also been discovered [e.g., *Gendrin et al.*, 2005; *Bibring et al.*, 2006; *Milliken et al.*, 2008; *Bandfield*, 2008; *Ehlmann et al.*, 2008; *Osterloo et al.*, 2008; *Murchie et al.*, 2009; *Wray et al.*, 2009; *Carter et al.*, 2010; *Ehlmann et al.*, 2011a, 2011b]. These examples reveal the presence of a dynamic sedimentary environment on the surface of ancient Mars.

The *Sprit*, *Opportunity*, and *Curiosity* rovers have each encountered sedimentary rocks along their traverses. The Mars Exploration Rover (MER), *Opportunity*, identified sulfate-rich, cross-bedded sandstones that contain hematite spherules at Meridiani Planum [*Squyres et al.*, 2004]. Based on the detailed mineralogy

and sedimentary facies observed, the rocks were interpreted as evaporites that have been reworked and mixed with basaltic clastic material, transported and lithified by evaporitic cements in a dune/interdune environment [*McLennan et al.*, 2005]. The spherules were interpreted to have formed through diagenetic fluids that remobilized iron within the evaporitic sandstone unit; subsequent erosion of the unit preferentially left a lag deposit of the more erosion-resistant spherules [*McLennan et al.*, 2005].

At Gusev Crater on Mars, there is a lack of extensive sedimentary units; however, some sulfate and carbonated-cemented rocks were encountered as float in the Columbia Hills. The instruments aboard the Mars Exploration Rover, *Spirit*, returned geological, geochemical, and mineralogical data from the Columbia Hills indicative of alteration products from an aqueous episode on the surface of Mars [*Squyres et al.*, 2006]. The "Peace Class" rocks of Columbia Hills have been interpreted as basaltic sandstones formed from the saturation of ultramafic sand with a sulfate rich fluid and eventual evaporation [*Squyres et al.*, 2006]. Furthermore, MER *Spirit* returned Miniature Thermal Emission Spectrometer data that indicated Mg-Fe-rich carbonates present in the Comanche outcrops in Columbia Hills [*Morris et al.*, 2010]. These outcrops represent a diverse aqueous history that altered only the top portion of an olivine-rich volcaniclastic Algonquin class, leaving behind a stratigraphy of a heavily altered and carbonate enriched upper unit, an unaltered lower unit, and an intermediate middle unit [*Ruff et al.*, 2014].

More recently, the Mars Science Laboratory *Curiosity* rover has encountered a succession of sedimentary rocks during its traverse at the landing site of Gale Crater. Yellowknife Bay has a rich sedimentary history that has been characterized in terms of mineralogy [*Vaniman et al.*, 2014], geochemistry [*McLennan et al.*, 2014], and stratigraphy [*Grotzinger et al.*, 2014]. The primary composition of the two mudstones sampled, John Klein and Cumberland, consists of detrital basaltic minerals, iron oxides and sulfides, calcium sulfates, smectites, and a substantial amorphous component [*Vaniman et al.*, 2014]. The data returned from Yellowknife Bay has led to a self-consistent interpretation of an ancient fluvial-lacustrine environment constrained by at least two distinct diagenetic episodes [*McLennan et al.*, 2014].

On Earth, compositional studies of sedimentary rocks provide a framework for understanding how tectonic, climatic, and biogeochemical processes have evolved over Earth's history [*McLennan et al.*, 1993]. The composition of sedimentary rocks has been used as a proxy to decipher Earth's geologic evolution and includes (but not limited to) such techniques as the quantification of feldspar alteration used to determine the extent of chemical weathering [*Nesbitt and Young*, 1982], the identification of secondary clay minerals to supply insight to diagenetic history [*Eberl et al.*, 1984], and the application of rare earth elements patterns to index provenance [*Taylor et al.*, 1981]. Furthermore, characterization of bulk mineralogy yields important information about source rocks, depositional environment, and diagenetic processes.

Given that the mineralogy is a key aspect in understanding chemical and physical conditions of sedimentary transport, deposition, and provenance, the expansion of remote sensing capability in determining rock composition becomes critically important. One of the techniques that is routinely used to estimate rock compositions remotely is thermal emission spectroscopy [e.g., *Bandfield et al.*, 2000; *Bandfield*, 2002; *Rogers and Christensen*, 2007; *Koeppen and Hamilton*, 2008]. This technique relies on the assumption that thermal emission spectra from each component within the mixture combine in proportion to their areal fraction to produce a bulk rock spectrum. A number of laboratory studies (section 2.2), mostly focused in igneous rocks and sands, have been conducted to validate the accuracy of mineral abundance derived from thermal emission spectra [*Feely and Christensen*, 1999; *Hamilton and Christensen*, 2000; *Wyatt et al.*, 2001; *Michalski et al.*, 2004]. However, studies focused on sedimentary materials have been limited [*Baldridge et al.*, 2004; *Michalski et al.*, 2006]. Because thermal emission spectra are influenced by not only composition but also particle size and compaction [e.g., *Salisbury and Wald*, 1992] (section 2.1), and because sedimentary rocks are commonly composed of small grain sizes and can exhibit different porosities than igneous rocks [e.g., *Manger*, 1963; *Wood and Fernandez*, 1988; *Sharma*, 2015], there is a need to characterize the spectral mixing behavior of naturally compacted fine-grained materials, such as those associated with sedimentation processes (i.e., sedimentary matrix materials), in detail.

The goal of this paper is to therefore assess the capability of thermal emission spectroscopy for the determination of the mineralogy of sandstones and mudstones in order to enhance our interpretations

of the Martian surface. We accomplish this by conducting a cross analysis of petrographic images and X-Ray diffraction (XRD) patterns in comparison with the mineral abundances derived from the bulk rock thermal emission (TIR) spectra of a suite of terrestrial sandstones and mudstones. In a companion paper by *Pan et al.* [2015], the spectral mixing behavior of synthetic compacted very fine-grained ($<$ ~10 μm) mixtures is assessed, and the applicability of partial least squares (PLS) analysis methods is presented.

2. Background

2.1. Thermal Emission Spectroscopy

Thermal emission spectroscopy, a form of vibrational spectroscopy, is sensitive to molecular bending and stretching vibrational modes present in any material. The frequencies of vibration (~100–10,000 cm^{-1}, or ~1–100 μm) are related to the chemical composition and structure of the mineral. Thermal emission spectroscopy is useful for geologic remote sensing applications because (1) individual minerals have unique and characteristic molecular vibrational bands [*Thomson and Salisbury*, 1993] and (2) it is a passive technique, as opposed to other techniques such as Raman and TIR reflectance spectroscopy.

Thermal emission spectra are also affected by particle size, porosity, and compaction, such that changes in spectral shape or spectral contrast (absorption depth) can occur. With decreasing grain size, particles become more transparent at wavelengths where the absorption coefficient (k) is low. This results in a longer path length for emitted photons to exit the surface of a particulate medium, and results in more opportunity for absorption, thus lowering the emissivity at those wavelengths [*Moersch and Christensen*, 1995]. This is also known as volume scattering [e.g., *Vincent and Hunt*, 1968; *Salisbury and Wald*, 1992]. In spectral regions where k is high, the surface of each grain is highly reflective [*Vincent and Hunt*, 1968; *Salisbury and Wald*, 1992; *Moersch and Christensen*, 1995]. So for a fine-particulate medium, there is a larger number of photon reflection events (meaning, emitted energy from one particle is reflected off an adjacent particle), in addition to the emitted energy from each particle, and thus an increase in measured emissivity compared to coarse particulates [*Aronson et al.*, 1967; *Moersch and Christensen*, 1995]. This is also known as a "cavity effect" [e.g., *Williams*, 1961. The grain size at which both effects begin to occur is generally $<$ ~60 μm, but depends on the magnitude of the absorption coefficient (k), and is wavelength-dependent. With compaction, both effects are less pronounced, and results in spectral shapes and contrast that are similar to that of larger grains [*Salisbury and Wald*, 1992]. However, as shown in paper 2, effects from volume scattering are still present.

For loose particulate (e.g., unpacked) fine-grained ($<$60 μm) *mixtures*, volume scattering causes nonlinear spectral mixing, resulting in inaccurate mineral abundance determinations from linear least squares models [*Ramsey and Christensen*, 1998]. But, the degree to which nonlinear mixing occurs in compacted fine-grained mixtures has not been examined in detail. Because compaction (or reduced porosity) is known to reduce multiple reflections and volume scattering from fine-particulate volumes [*Salisbury and Wald*, 1992], one might expect that naturally compacted sediments and cemented mudstones and sandstones would show different mixing behavior than noncompacted fine-grained sediments. It is also unclear how the spectral mixing behavior of compacted fine-grained sediments might differ from that of a fine-grained crystalline igneous rock. As described in section 2.2, TIR-derived mineral abundances for basalts and andesites are generally accurate to within ~15 vol % [*Hamilton and Christensen*, 2000; *Wyatt et al.*, 2001]. But because some mudstones and sandstones can have differing porosities than basalts, we might expect differences in spectral mixing behavior. The above discussion provides the motivation behind this work. Below, we review previous thermal emission laboratory studies of rocks.

2.2. Previous Thermal Emission Studies on Rocks

Using the laboratory thermal emission measurement techniques described by *Ruff et al.* [1997], thermal emission spectral libraries of many common rock-forming minerals were developed [*Christensen et al.*, 2000]. These libraries were then used to test the validity of mineral mixing in multicomponent samples. *Ramsey and Christensen* [1998] used a deconvolution and linear retrieval algorithm to investigate the spectral behavior of minerals in a mixture. Using a chi-square minimization technique, they were able to model and accurately identify up to 15 minerals in a mixture of sand-sized particles or larger, to accuracies within 5%

(absolute) on average [*Ramsey and Christensen*, 1998], demonstrating that components in a sample spectrum contribute to the overall spectrum in proportion to their areal abundance.

Feely and Christensen [1999] investigated the thermal emission spectral mixing behavior of 45 igneous and 51 metamorphic rocks, in which they concluded that the derived mineral abundances for primary minerals (feldspars, quartz, pyroxene, and carbonates) were within 7–15% of the optically determined abundances. Subsequently, *Hamilton and Christensen* [2000] obtained similar results for 20 mafic and ultramafic rocks by recovering modal mineralogy within 5–15% for 92% of their samples; and investigation of 28 terrestrial basalts and andesites returned absolute differences ranging from 2.4 to 12.2 vol % [*Wyatt et al.*, 2001]. *Michalski et al.* [2004] studied 46 weathered granitic rocks that resulted in mineral abundances within 0–15% of the petrologically determined modes. However, not all rocks demonstrate linear mixing behavior. From examination of TIR spectra of evaporites, *Baldridge et al.* [2004] concluded that samples containing a significant amount of halite, which is a TIR transparent material, and (or) fine-grained particulates, result in an increased volume scattering effect and thus an unsatisfactory model. Similar results were determined from the analysis of 22 clay-bearing rocks, where *Michalski et al.* [2006] determined that linear unmixing of TIR spectra can provide adequate clay-bearing rock mineral abundances estimates (within ~5%), but the identification of individual clay minerals is insufficient within an intimate mixture of clay-sized grains.

These studies established a foundation for the interpretation of orbital and rover data, but there still remains a knowledge gap in the spectral characterization of sedimentary rocks. In particular, the TIR spectral behavior of mudstones with a widely ranging mixture of silt and clay-sized particles ($<$62.5 μm), and sandstones consisting of larger sand-sized grains ($>$62.5 μm and $<$2 mm) cemented with a matrix component of silt and clay-sized particles, has yet to be characterized. The widespread sedimentary units identified from orbit and landed missions (section 1) make the study of sedimentary rock thermal emission features critically important for the future of Mars research.

3. Methods

3.1. Sample Description and Preparation

The sedimentary rocks used for this investigation consist of a previously well-characterized set of sandstones and mudstones and are intended to span a wide range of compositions and grain size. Although these samples, which contain significant quartz and feldspar components, are not perfect analogs to the sedimentary rocks of Mars, they are useful for demonstrating the mixing relationships between clastic rocks components.

Sandstones were acquired from the Stony Brook University Geosciences Department's Sedimentary Rock Collection. In addition, we also included a basaltic sandstone from Carapace Nunatak, Antarctica, described in *Cannon et al.* [2015] (Table 1). These sandstone samples used for this investigation span a wide range of composition, with general classifications spanning from arkose arenites to lithic graywackes. Furthermore, sandstone grain size and textural maturity is variable, with modal grain sizes extending from very fine to coarse sand (section 3.2.3); angularity and sorting vary between each sample.

Mudstone samples from the Huronian Supergroup (2.5–2.2 Ga) outcrop belt on the northern shore of Lake Huron, Canada, were donated by Scott McLennan. The Huronian Supergroup sequence experienced deformation and low-grade metamorphism (subgreenschist grade) during the Penokean Orogeny (1.85–1.80 Ga), resulting in meta-sedimentary rocks with recrystallization of micas (i.e., increased grain size) and albitization products. Thus, the texture of our samples may differ from sedimentary rocks on Mars, where burial and exhumation may be less common. Nevertheless, they provide a good first-order approximation of expected spectral mixing behavior for mudstones, in general. Mudstones from this sequence (Table 1) were initially geochemically and petrographically characterized by *McLennan et al.* [1979], who determined that the samples exhibit similar mineralogical content but obvious variations in matrix and framework mineral abundances. *McLennan et al.* [1979] categorized these mudstones into three broad groups based upon the content of their matrix and framework minerals: a sericite rich matrix group, a sericite rich matrix but framework mineral feldspar-depleted group, and a chlorite rich matrix group.

Table 1. Rock Samples Used in This Investigation[a]

Sample Name	Formation	Sample Source Description[b]	Rock Type	Modal Clasts Grain Size (μm)	Sample Description
La Boca	La Boca	SBU	Sandstone	300	Tan to brown sandstone with rounded to subangular and moderately sorted grains
Tx-Te-1	-	SBU	Sandstone	300	Gray sandstone with rounded to subangular and poorly sorted grains
16-606	-	SBU	Sandstone	100	Gray sandstone with subrounded to well-rounded and well-sorted grains
Catskill SK-1	Catskill	SBU	Sandstone	300	Dark gray sandstone with subangular to subrounded and poorly sorted grains
DI-72-91	-	SBU	Sandstone	200–400	Gray sandstone with subrounded and well-sorted grains
Devil K	-	SBU	Sandstone	200	Tan sandstone with-round and well-sorted grains
Smithwick	Smithwick	SBU	Turbidtic Sandstone	300	Gray sandstone with subangular to subrounded and well-sorted grains
Mis-Te-2	-	SBU	Sandstone	250	Red sandstone with sub angular and well sorted grains
Flatirons	Fountain	MTT	Sandstone	400–700	Red sandstone with subangular and poorly sorted grains
Berea	Berea	WARDS	Sandstone	200–300	Gray sandstone with angular to subangular and moderately sorted grains
Gratton	Gratton	WARDS	Sandstone	100–400	Graywacke with angular to subangular and poorly sorted grains
Mt. Tom	Sugarloaf	WARDS	Sandstone	500	Arkoses with subangular and poorly sorted grains
Carapace	Carapace Sandstone	KMC	Sandstone	100	Light gray sandstone with subrounded detrital grains
SM-75-142	McKim	SMM	Claystone	1.95–4	Gray clayey shale with silt laminae
SM-75-120	McKim	SMM	Mudstone	1.95–62.8	Gray mudstone
SM-75-117	Pecors	SMM	Sandy clayey siltstone	1.95–4	Gray clayey shale with silt-very fine sand laminae
SM-75-107	Gowganda	SMM	Clayey mudstone	1.95–4	Gray clayey laminated mudstone
SM-75-104	Gowganda	SMM	Mudstone	1.95–62.8	Gray clayey laminated mudstone
SM-75-134	Gowganda	SMM	Siltstone	4–62.8	Gray silty mudstone
SM-75-115	Pecors	SMM	Mudstone	4–62.12	Gray mudstone
SM-75-140	Gordon Lake	SMM	Sandy mudstone	4–62.8	Gray laminated mudstone
SM-75-158	Gordon Lake	SMM	Silty mudstone	4–62.8	Gray silty laminated mudstone
SM-75-113	McKim	SMM	Mudstone	1.95–62.8	Gray mudstone
SM-75-105	Gowganda	SMM	Mudstone	1.95–62.8	Gray clayey shale with silt laminae
SM-75-103	Gowganda	SMM	Mudstone	1.95–62.8	Gray clayey shale with silt laminae
SM-75-165	Gowganda	SMM	Sandy mudstone	1.95–62.8	Dark gray clayey shale with silt-very fine sand laminae
SM-75-123	Pecors	SMM	Mudstone	1.95–62.8	Dark gray clayey shale

[a]Source abbreviations: SBU, Stony Brook University; WARDS, Ward's Science; SMM, Scott McLennan; KMC, Kevin Cannon; MTT, Michael Thorpe. Formation listed if known.
[b]Sandstone grain size is determined from the average length of clasts diameter, as measured under a petrologic microscope. Mudstone modal grain size is determined by the same procedure, but due to the increasingly small grain size, measurements are confirmed with micro-Raman images.

Sample preparation is typically not required for thermal emission spectroscopy, but in order to analyze the same localities within each sample, freshly cut surfaces were prepared. We cut the samples to approximately $4.5 \times 2.5 \times 1.5$ cm sizes to produce a thick section for TIR analysis. Thin sections from the same location on the sample's surface were analyzed by point counting techniques. For sandstones, modal grain size was determined by measuring the mean diameter of at least 100 detrital clasts (Table 1). Similarly, mudstone grain size was determined by the same procedure, but due to the small clasts, grain size was also confirmed using micro-Raman images. The micro-Raman spectrometer combines a confocal microscope with a 785 nm laser, resulting in submicron spot size, and thus allowing for detailed images of clay-sized grains.

Table 2. Sedimentary Mineral Library Composed of Mineral Spectra From the Arizona State University's (ASU) Spectral Library

Mineral Group	TIR Library ID[a]
Amphibole	Anthophyllite BUR-4760
	Glaucophane WAR-0219
	Hornblende BUR-2660
	Magnesiokatophorite ASU-03
	Pargasite HS-177.4B
	Tremolite var. jade (Nephrite) WAR-0979
Carbonate	Aragonite (long-axis oriented) C11
	Calcite (Iceland Spar) ML-C2
	Calcite C27
	Calcite C40
	Calcite ML-C10
	Cerussite C51
	Dolomite C17
	Dolomite C28
	Fe66Mg34CO3 C56
	Kutnahorite C43
	Magnesite C55
	Mg54Fe39CO3 C5
	Micrite, slope adjusted[i]
	Minrecordite C23
	Siderite C50
	Smithsonite C30
	Smithsonite ML-C1
	Witherite C52
Clinopyroxene	Augite BUR-620
	Augite HS-119.4B
	Augite NMHN-122302
	Augite NMNH-119197
	Augite NMNH-9780
	Diopside NMNH-107497
	Diopside WAR-6474
	Hedenbergite manganoan DSM-HED01
	Hedenbergite manganoan NMNH-R11524
	Hedenbergite WAR-HED01
Epidote	Epidote BUR-1940
Garnet	Almandine BUR-120A
Glass	Si-K2O Glass[h]
	Quenched Basalt[h]
	Silica Glass[h]
	Flourite
Halide	Flourite BUR-2080C
	Sylvite[e]
K-Feldspar	Anorthoclase WAR-0579
	Microcline BUR-3460
	Orthoclase WAR-RGSAN01
	Perthite WAR-5802
Olivine	Fayalite WAR-RGFAY01
	Forsterite AZ-01
	Forsterite BUR-3720A
	KI 3008 Fo10[j]
	KI 3115 Fo68[j]
	KI 3362 Fo60[j]
	KI 3373 Fo35[j]
Orthopyroxene	Bronzite BUR-1920
	Bronzite NMNH-119793
	Bronzite NMNH-93527
	Enstatite DSM-ENS01
	Enstatite NMNH-34669
	Enstatite NMNH-82436
	Enstatite NMNH-R14440

3.2. Analytical Technique

3.2.1. Spectrometer Setup and Spectra Collection

Thermal emission spectra were collected at the Stony Brook University Vibrational Spectroscopy Laboratory using a Thermo Fisher Nicolet 6700 Fourier transform infrared Michelson interferometer that has been modified to directly measure emitted energy by removing the internal infrared source. The apparatus setup and the spectra collection technique follow closely to that described by *Ruff et al.* [1997]. The sample's emitted radiance was acquired over a spectral range of 4000–200 cm^{-1} (2.5–50 μm) at a sampling of 2 cm^{-1}. During an approximately 8 min acquisition period, 256 interferograms were collected at an optical velocity of 0.4747 cm^{-1}. Following an optical path directed by parabolic mirrors, emitted photons pass through a cesium iodide beam splitter and are finally sensed by a deuterated triglycine sulfate detector. Rock samples were heated in an oven set at 80°C for at least 6 h. In order to increase the signal-to-noise ratio, samples were actively heated (80°C) throughout the acquisition period. The spectrometer and sample chamber (contained within a glovebox) are purged with air scrubbed of water vapor and CO_2, in an effort to mitigate the presence of water vapor and CO_2 absorptions in the measured spectra [*Ruff et al.*, 1997]. The sample chamber, constructed of copper and painted with high emissivity black paint in the interior, allows the environmental (downwelling) radiance to be regulated by circulating water at a controlled temperature of 20°C during the sample collection period [*Mathew et al.*, 2009]. Depending on sample size, the typical measurement spot diameter ranged from 1 to 1.5 cm, with coarser-grained samples requiring a larger spot size to accurately capture bulk composition [*Michalski et al.*, 2004]. Before each session (four samples per session), the measurement of a warm and hot blackbody (70°C and 100°C, respectively) was

Table 2. (continued)

Mineral Group	TIR Library ID[a]
	Hypersthene DSM-FER01
Oxides	Magnetite WAR-0384
	Hematite BUR-2600
	Goethite-Derived Hematite GTSH2-300[f]
	"Specular Goethite WAR-G1, 710–1000 μm[f]
	Synthetic Packed Goethite Powder GTS4[f]
	Synthetic Packed Magnetite Powder MTS4[f]
Phosphate	Apatite (perp. to c-axis) ML-P1
	Apatite ML-P1
	Apatite ML-P2
	Meta-variscite ML-P8
	Pyromorphite ML-P3
	Pyromorphite ML-P6
	Turquoise ML-P5
	Wavellite ML-P7
	Albite (Cleavelandite) WAR-0612
Plagioclase	Albite WAR-0235
	Andesine BUR-240
	Andesine WAR-0024
	Anorthite BUR-340
	Anorthite WAR-5759
	Bytownite WAR-1384
	Labradorite BUR-3080A
	Labradorite WAR-4524
	Labradorite WAR-RGAND01
	Oligoclase BUR-060
	Oligoclase WAR-0234
Quartz	jasper
	novaculite_natural
	Quartz BUR-4120
	Herckimer_qtz_xlface_a-axis, slope adjusted
Serpentine	Serpentine HS-8.4B
Sheet-silicates	Illite granular IMt-2, scaled 130%
	Nau-1 < 0.2 mic[d]
	nau-2 < 0.2 mic[d]
	saponite < 0.2 mic
	Sbdl < 0.2 mic
	Swy-1 < 0.2 mic
	Clinoptilolite 27031[g]
	Mordenite 27133[g]
	Clinochlore[g]
	Kaolinite KGa-1b
	Nontronite NAu-1[g]
	Nontronite NAu-2[g]
	Palygorskite PFl-1
	Saponite SapCa-2[g]
	Montmorillonite SAz-1[g]
	Beidellite SBCa-1[g]
	Montmorillonite SCa-3[g]
	Sepiolite SepSp-1[g]
	Hectorite SHCa-1[g]
	Montmorillonite STx-1[g]
	Montmorillonite SWy-2
	Synthetic Clay Syn-1[g]
	Biotite BUR-840
	Chlorite WAR-1924
	Clinochlore BUR-1340
	Muscovite WAR-5474
Silica	02-011 Opal A ¤[c]
	02-015 Opal-CT/C ¤[c]
	Cristobalite ¤[c]
Sulfate	Anhydrite 755

obtained from a solid aluminum conical cavity (painted with high heat flat black paint) that was attached to the chamber apparatus [*Ruff et al.*, 1997]. The blackbody measurements are used to generate the instrument response function and calibrate the sample radiance measurement. Sample emissivity is derived from spectral radiance using the method described by *Realmuto* [1990] and *Christensen* [1998]. This technique has been previously proven to have a emissivity reproducibility of better than 1% and an accuracy of better than 2% [*Ruff et al.*, 1997].

3.2.2. Spectral Modeling

The emissivity spectra of individual rock samples were modeled with mineral spectra using a form of nonnegative linear least squares (NNLS) minimization that was previously used by *Rogers and Aharonson* [2008] and is based on methods presented in *Lawson and Hanson* [1974]. For a mixed spectrum (i.e., the rock sample spectrum) $Y(\lambda)$, and a matrix of input library spectra $X(\lambda)$ of length n, the model solves the equation

$$Y(\lambda) = \sum_{i=1}^{n} \beta_i X(\lambda)_i + \delta(\lambda) \qquad (1)$$

where β_i is the vector of coefficients for each library spectrum and λ is the wavelength. The residual error between the measured spectrum (Y) and modeled spectrum $\left(\sum \beta_i X(\lambda)_i\right)$ is represented as $\delta(\lambda)$. To avoid negative values of β_i, which have no geological meaning, the NNLS method we use here allows for all spectra to remain in the matrix until a final best model using only nonnegative coefficients is achieved [*Rogers and Aharonson*, 2008]. The model inputs are the rock sample spectrum and a library of potential spectral end-members (described in detail below), which includes a blackbody end-member to account for spectral contrast differences between rock and library spectra [*Hamilton et al.*, 1997]. The output is the modeled spectrum, library spectra coefficients (β_i), and a root-mean-square (RMS) of the difference between the measured and modeled spectra. Next, mineral abundances are

Table 2. (continued)

Mineral Group	TIR Library ID[a]
	Antlerite ML-S10
	Barite ML-S2
	Bassanite 757
	Celestite ML-S3
	Gypsum 758
	Gypsum var. Alabaster ML-S11
	Anhydrous Magnesium Sulfate[e]
	Kieserite[e]
	Pentahydrite[e]
	Sanderite[e]
	Starkeyite[e]
Zeolite	Crystalline heulandite (zeo)[b]
	Crystalline stilbite (zeo)[b]

[a]Except where indicated, all library spectra are from the ASU spectral library (tes.asu.edu) [*Christensen et al.*, 2000].
[b]*Ruff et al.* [2006].
[c]*Michalski et al.* [2006].
[d]*Michalski et al.* [2003].
[e]*Baldridge* [2008].
[f]*Glotch et al.* [2004].
[g]*Che and Glotch* [2012].
[h]*Wyatt et al.* [2001].
[i]*Hardgrove and Rogers* [2014].
[j]*Koeppen and Hamilton* [2008].

determined by subtracting the blackbody coefficient from the sum of β_i, and renormalizing the remaining coefficients in β_i, to sum to 100% [*Feely and Christensen*, 1999; *Hamilton et al.*, 1997; *Wyatt et al.*, 2001]. The spectral modeling range for our samples was set from 1650 to 230 cm^{-1}, covering the major spectral features of all of our samples as well as all phases in our input library [*Hamilton and Christensen*, 2000].

A sedimentary spectral library was constructed using spectra from a number of sources (Table 2) and was designed to include all major phases that could potentially be present within a sedimentary rock. The library consisted of 135 mineral spectra collected from sand-sized or larger particles, or, for the case of clays, pressed pellets. A larger spectral library is ideal for investigating samples of unknown composition, but there was some concern that a too-large library might reduce model accuracy [e.g., *Rogers and Aharonson*, 2008]. To determine the effect of library size, we also created a controlled library with only phases known to be present and found the model results to be within approximately 5% of those from the larger library, on average. Thus, results presented in this study are from the larger library. Spectral plots in this work show the measured sample spectrum, the modeled spectrum,

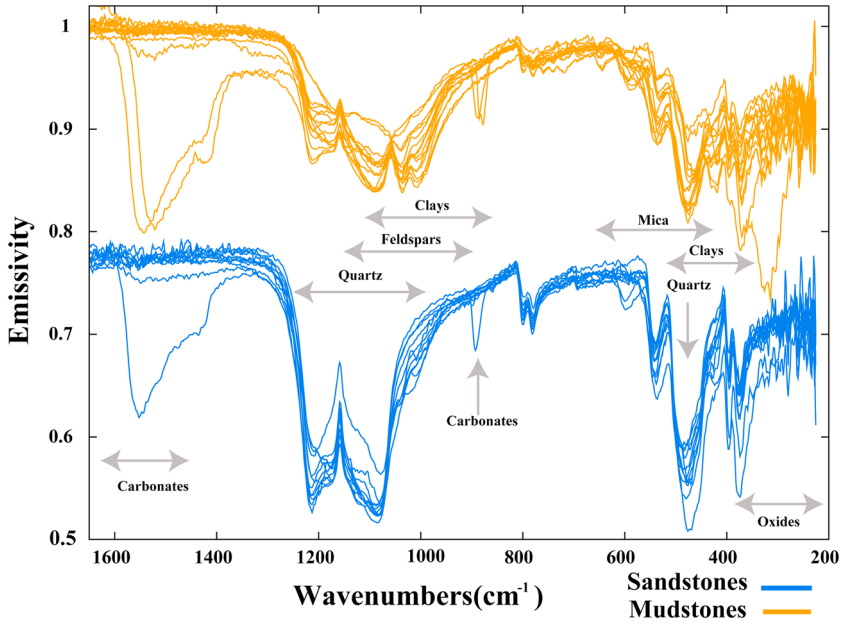

Figure 1. The measured emissivity spectra for all sandstones and mudstones, with highlighted mineral group contributions determined from general location of absorption features. Major differences between sandstone and mudstone TIR spectra are mainly observed from ~1250 to 1000 cm^{-1}, primarily due to differences in clay abundance. Carbonate features are present in some samples between ~1550 and 1450 cm^{-1}. The prominent absorptions between ~1300 and 1050 cm^{-1} are due to quartz contributions.

Table 3. Sandstone TIR Mineral Volume Abundances Derived From the Nonnegative Least Squares (NNLS) Unmixing Algorithm[a,b]

	Carapace	Mt. Tom	Gratton	Berea	Flat Irons	Smithwick	Catskill	DI-72-91	Devil K	Tx-Te-1	Mis-Te-2	La Boca	16-606
Amphibole	0.66 ± *0.73*	2.17 ± *0.90*	0.00 ± *0.00*	0.00 ± *0.00*	0.00 ± *0.00*	0.00 ± *0.00*	2.57 ± *0.92*	0.39 ± *0.72*	0.00 ± *0.00*	0.13 ± *0.79*	0.00 ± *0.00*	14.78 ± *1.59*	1.28 ± *0.77*
Carbonate	1.22 ± *0.27*	1.10 ± *0.29*	41.56 ± *0.78*	7.87 ± *0.53*	1.14 ± *0.21*	2.13 ± *0.48*	1.80 ± *0.44*	2.10 ± *0.34*	0.69 ± *0.40*	0.69 ± *0.43*	0.84 ± *0.66*	1.52 ± *0.38*	3.17 ± *0.55*
Clay	1.51 ± *0.87*	6.57 ± *4.62*	0.00 ± *0.00*	0.58 ± *0.00*	9.88 ± *0.00*	3.92 ± *0.00*	5.78 ± *0.00*	0.28 ± *0.00*	0.71 ± *0.00*	6.80 ± *0.00*	17.91 ± *0.00*	13.64 ± *0.00*	13.63 ± *0.00*
Clinopyroxene	0.00 ± *0.00*	2.14 ± *1.93*	0.25 ± *0.51*	0.00 ± *0.00*	0.00 ± *0.00*	0.00 ± *0.00*	0.00 ± *0.00*	0.00 ± *0.00*	2.40 ± *0.71*	0.00 ± *0.00*	0.36 ± *0.87*	0.68 ± *1.27*	0.00 ± *0.00*
Epidote	0.00 ± *0.00*	0.00 ± *0.00*	0.00 ± *0.00*	0.00 ± *0.00*	0.00 ± *0.00*	0.00 ± *0.00*	0.00 ± *0.00*	0.00 ± *0.00*	0.00 ± *0.00*	0.00 ± *0.00*	0.00 ± *0.00*	0.00 ± *0.00*	0.00 ± *0.00*
Garnet	0.00 ± *0.00*	0.00 ± *0.00*	0.00 ± *0.00*	0.00 ± *0.00*	0.00 ± *0.00*	0.00 ± *0.00*	0.00 ± *0.00*	0.00 ± *0.00*	0.00 ± *0.00*	0.00 ± *0.00*	0.00 ± *0.00*	0.46 ± *0.41*	0.00 ± *0.00*
Glass and Silica	0.00 ± *0.00*	0.00 ± *3.00*	0.00 ± *0.00*	6.83 ± *1.43*	0.00 ± *1.89*	0.09 ± *6.83*	11.37 ± *4.25*	0.00 ± *0.99*	0.00 ± *1.06*	26.70 ± *2.47*	0.00 ± *1.19*	0.00 ± *1.01*	5.30 ± *1.57*
Halide	0.00 ± *0.00*	5.67 ± *0.00*	0.20 ± *0.00*	0.00 ± *0.00*	0.00 ± *0.00*	0.20 ± *0.00*	0.18 ± *0.00*	0.07 ± *0.00*	0.00 ± *0.00*	0.26 ± *0.00*	0.00 ± *0.00*	6.37 ± *0.00*	2.29 ± *0.00*
K-Feldspar	3.32 ± *1.21*	0.00 ± *2.94*	0.00 ± *0.27*	0.00 ± *0.00*	25.56 ± *0.00*	0.00 ± *0.27*	0.00 ± *0.29*	4.93 ± *0.85*	0.00 ± *0.00*	0.13 ± *0.21*	0.00 ± *0.00*	0.00 ± *0.32*	0.00 ± *0.25*
Mica	0.00 ± *0.00*	1.38 ± *0.00*	0.00 ± *0.00*	0.00 ± *0.00*	0.00 ± *0.91*	0.00 ± *0.00*	0.31 ± *0.00*	0.70 ± *1.13*	0.00 ± *0.00*	0.00 ± *1.14*	0.00 ± *0.00*	0.00 ± *0.00*	0.00 ± *0.00*
Olivine	0.00 ± *0.00*	3.56 ± *0.43*	0.00 ± *0.00*	0.00 ± *0.00*	0.00 ± *0.00*	0.00 ± *0.00*	0.00 ± *0.76*	0.00 ± *0.60*	0.00 ± *0.00*	1.11 ± *0.00*	0.00 ± *0.00*	0.22 ± *0.00*	0.00 ± *0.00*
Orthopyroxene	0.14 ± *0.00*	4.47 ± *3.01*	0.00 ± *0.00*	0.00 ± *0.00*	0.00 ± *0.00*	0.00 ± *0.00*	0.00 ± *0.00*	0.00 ± *0.00*	0.00 ± *0.00*	0.00 ± *0.30*	0.00 ± *0.00*	0.00 ± *1.19*	0.00 ± *0.00*
Oxide	0.00 ± *0.31*	2.18 ± *0.41*	0.95 ± *0.00*	0.00 ± *0.00*	0.84 ± *0.00*	1.46 ± *0.00*	2.53 ± *0.00*	0.27 ± *0.00*	1.76 ± *0.00*	1.46 ± *0.00*	0.62 ± *0.00*	9.58 ± *0.00*	0.00 ± *0.00*
Phosphate	3.48 ± *1.39*	6.16 ± *1.14*	0.00 ± *0.64*	0.00 ± *0.00*	5.15 ± *0.56*	8.56 ± *0.34*	11.73 ± *0.60*	3.10 ± *0.31*	6.27 ± *0.94*	2.53 ± *0.43*	8.79 ± *0.43*	0.00 ± *0.85*	9.15 ± *0.00*
Plagioclase	26.98 ± *2.00*	20.55 ± *2.93*	0.00 ± *0.00*	0.00 ± *0.00*	5.45 ± *1.22*	1.62 ± *1.96*	1.91 ± *2.49*	26.83 ± *1.41*	0.00 ± *1.62*	10.77 ± *1.19*	0.78 ± *1.85*	7.05 ± *0.00*	6.14 ± *1.29*
Quartz	44.03 ± *0.42*	27.52 ± *0.53*	50.25 ± *0.00*	64.50 ± *0.00*	43.34 ± *1.35*	76.46 ± *0.56*	60.57 ± *1.12*	52.56 ± *2.03*	74.17 ± *0.00*	38.49 ± *2.10*	61.40 ± *0.87*	45.69 ± *0.98*	51.11 ± *1.03*
Serpentine	0.00 ± *0.00*	16.52 ± *0.00*	0.00 ± *0.44*	0.00 ± *0.67*	0.00 ± *0.42*	0.00 ± *0.63*	0.00 ± *0.73*	0.00 ± *0.50*	0.00 ± *0.67*	0.00 ± *0.51*	0.00 ± *0.60*	0.00 ± *0.49*	0.00 ± *0.55*
Sulfate	18.64 ± *1.16*	0.00 ± *1.36*	6.79 ± *0.84*	20.23 ± *1.08*	8.64 ± *1.04*	5.57 ± *0.74*	1.25 ± *1.01*	8.77 ± *1.95*	13.97 ± *1.37*	8.91 ± *1.60*	9.29 ± *0.72*	0.00 ± *0.00*	7.93 ± *1.31*
Zeolite	0.00 ± *0.00*	0.00 ± *0.00*	0.00 ± *0.00*	0.00 ± *0.00*	0.00 ± *0.00*	0.00 ± *0.00*	0.00 ± *0.00*	0.00 ± *0.00*	0.00 ± *0.00*	2.02 ± *2.33*	0.00 ± *0.00*	0.00 ± *0.00*	0.00 ± *0.00*

[a]Statistical errors from the NNLS are italicized below mineral group abundances [*Rogers and Aharonson*, 2008].
[b]Silica and glass abundances are grouped together due to their remarkably similar spectral shapes [*Glotch et al.*, 2006].

the individual end-member contributions to the model (scaled by modeled abundance), and the difference between the model and the measured (δ) in comparison to a zero reference point indicating perfect fit.

The uncertainties given for TIR models are standard errors of coefficients from the least squares minimization routine [*Rogers and Aharonson*, 2008]. These numerical errors are dependent on the other phase abundances returned from the model but do not account for systematic errors associated with missing end-members, inaccurate particle size of end-members, or nonlinear mixing associated with smaller grain sizes. Assessment of those uncertainties comes from the comparison with the other techniques used for this investigation (section 5) and is one of the general goals of this paper.

3.2.3. Optical Point Counts

Modal composition from thin sections of samples with an average grain size of fine sand or larger (>100 μm) was determined optically using a petrographic microscope. For any samples with a smaller average grain size, accurate identification of minerals by optical petrology becomes increasingly difficult [*Williams et al.*, 1954]. Sandstones were the main rock types meeting the criteria for a petrographic analysis; however, all samples were examined under a petrologic microscope to qualitatively assess texture and grain size, as well as provide a rough independent check on abundances obtained through the other quantitative mineralogy techniques employed in this study. In total, 13 samples were examined by traditional point counting practices in order to establish their bulk mineralogy. Modal mineralogy determined from point counts were conducted prior to acquisition of TIR spectra to avoid bias.

Sandstone petrographic methods have evolved over time; different techniques are discussed in detail by *Weltje and von Eynatten* (2004). For this study, the sample thin section was

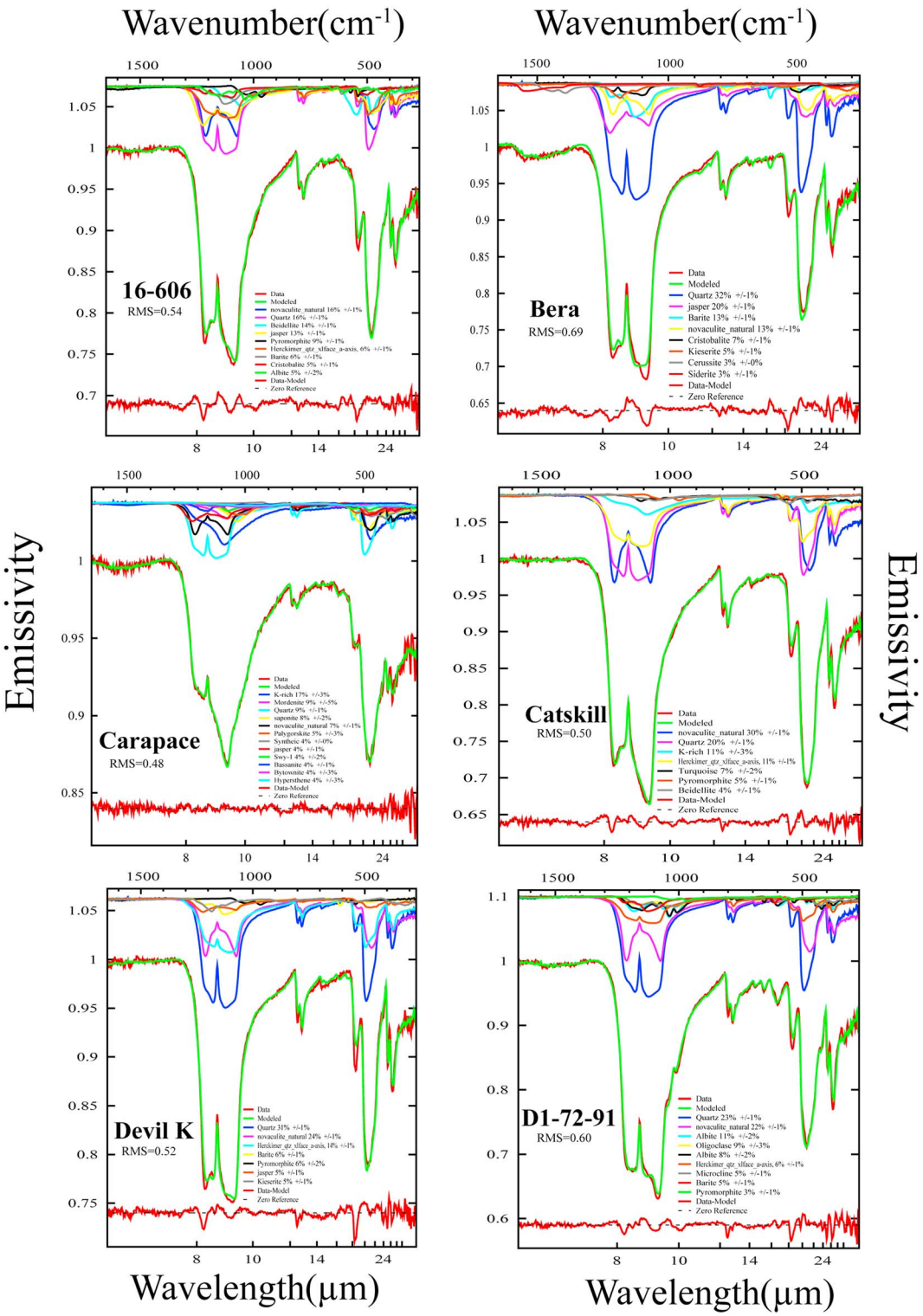

Figure 2. Measured versus modeled TIR emission spectra of 13 sandstones. Only individual mineral phases with abundances ≥ 3 vol % are displayed. In general, RMS values indicate a good fit between the measured and modeled spectra. Any deviation from a one-to-one relationship is highlighted using a zero reference line.

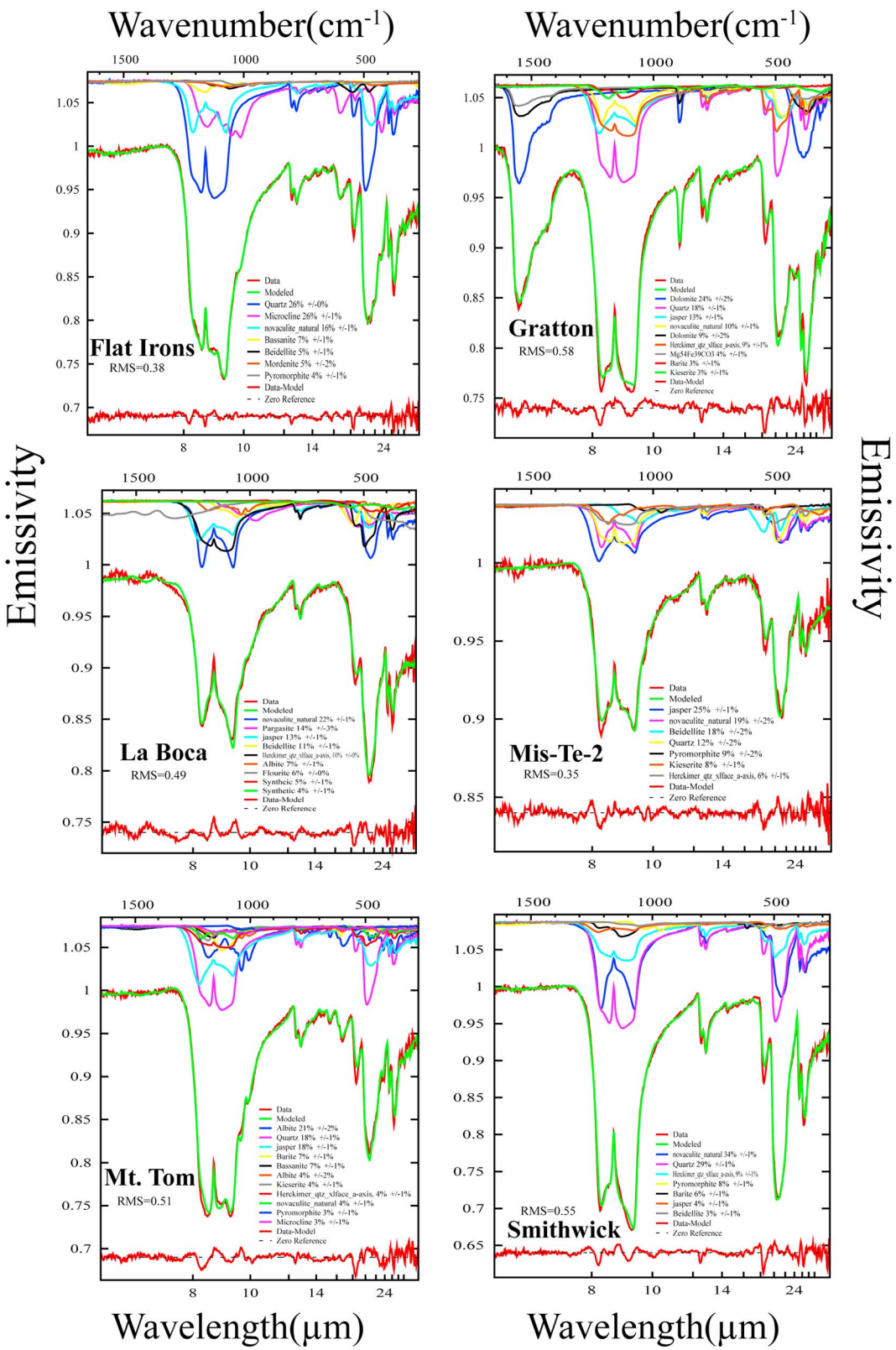

Figure 2. (continued)

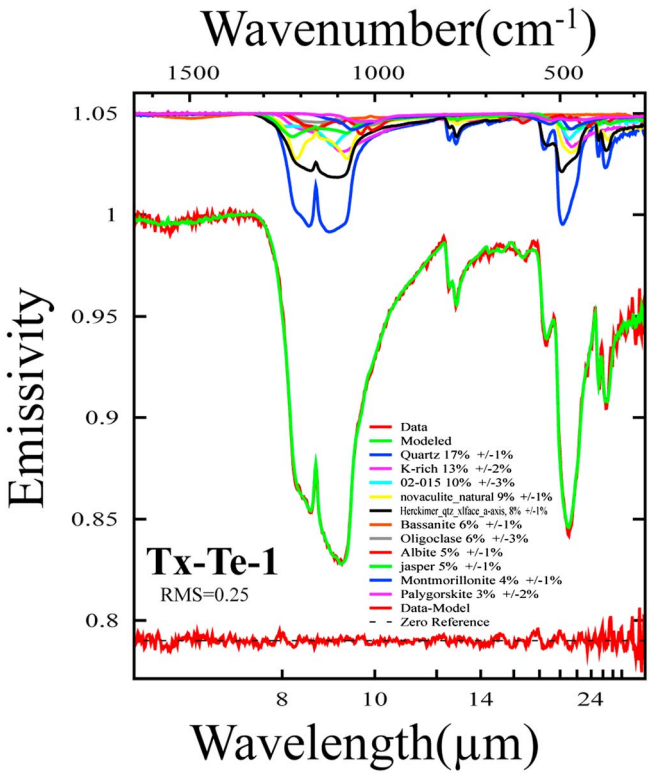

Figure 2. (continued)

systematically scanned and approximately 250 grains were identified at an average step of 1.5 times the modal clast grain size (unique to each sample), covering the entire 4.0 × 2.5 cm slide. Modal grain size was determined by averaging the diameter of approximately 100 clasts within each sample. Total rock composition was determined from the proportion that each mineral phase was identified within the ~250 points. This method should result in less than 6% absolute error, as determined from the chart for judging the reliability of point counting developed by *Van Der Plas and Tobi* [1965]. This uncertainty is comparable to the other quantitative techniques used for the determination of bulk mineralogy within this study.

Individual grains were optically identified beneath the cross hairs of the microscope and then classified into their respective sedimentary rock mineral phase. These mineral phases replicate the selection of library mineral spectra used as inputs to spectral models. Cement and matrix phases were generalized into a single "matrix" group based upon common optical features (i.e., texture, color, and grain boundary behavior).

3.2.4. Quantitative X-ray Diffraction

Powdered X-ray diffraction was completed using a Rigaku SmartLab Automatic X-ray Diffractometer system located at NASA Ames Research Center in Moffett Field, California. Samples were prepared for analysis following the procedures of *Eberl* [2003]. In summary, samples were mixed with 20 wt % corundum and milled into a fine powders (~5 μm) in ethanol using a McCrone mill and zirconium grinding elements. After drying, milled powders were shaken in plastic vials containing three plastic beads with ~0.5 mL of Vertrel, a fluorocarbon used as grinding medium to achieve a grain size below 10 μm, for approximately 10 min. This procedure produces spherical aggregates of powder that reduce preferred mineral orientation during side-loading into XRD sample holders [*Środon et al.*, 2001]. XRD patterns were acquired using Cu K-alpha radiation (40 kV, 40 ma) from 5 to 65 degrees 2-theta with a scintillation counter at 0.02 degree steps, at 4 s per step. After phase identification from XRD profiles, mineral abundances were determined by using whole-pattern fitting, using a custom program, based on and using the standards of RockJock [*Eberl*, 2003]. XRD weight abundances were then converted to volume abundances in order to allow for a direct comparison to the other techniques used in this study. X-ray diffraction errors are generally low, and in the case of whole-pattern fitting are associated with differences between the chemistry and structure of mineral standards and constituents of samples and differences in the geometry of the XRD instrument used to measure samples and standards. For major crystalline phases, which constitute more than 10 wt % , the uncertainty is generally $<$5 wt % (absolute) [*Środon et al.*, 2001].

4. Results

4.1. TIR Spectral Characteristics and Modal Mineralogy

Thermal infrared emission spectra of sandstones and mudstones display absorptions that are characteristic of component crystal structures and can be categorized based on wavelength position and shape (Figure 1). All sandstones have similar spectral shapes as a result of the fundamental vibration of anion groups. The prominent absorption doublet that occurs between ~1300 and 1050 cm^{-1} in all of the measured sandstone

Table 4. Mudstone TIR Mineral Volume Abundances Derived From the Nonnegative Least Squares (NNLS) Unmixing Algorithm[a,b]

	SM-75-140	SM-75-115	SM-75-123	SM-75-103	SM-75-165	SM-75-113	SM-75-105	SM-75-142	SM-75-120	SM-75-104	SM-75-107	SM-75-158	SM-75-134	SM-75-117
Amphibole	3.08 ± *1.41*	11.42 ± *1.49*	9.78 ± *1.19*	8.60 ± *1.32*	1.52 ± *0.62*	11.34 ± *0.99*	4.03 ± *0.86*	11.14 ± *1.23*	16.69 ± *1.60*	10.86 ± *1.32*	0.00 ± *0.00*	1.16 ± *0.64*	9.92 ± *1.00*	11.31 ± *1.44*
Carbonate	3.58 ± *0.52*	3.95 ± *0.49*	2.23 ± *0.24*	2.33 ± *0.48*	3.05 ± *0.47*	2.13 ± *0.42*	5.08 ± *0.43*	3.07 ± *0.51*	3.05 ± *0.71*	3.86 ± *0.57*	3.41 ± *0.43*	47.58 ± *0.55*	2.48 ± *0.26*	1.82 ± *0.30*
Clay	14.45 ± *3.24*	10.86 ± *1.84*	12.22 ± *0.00*	12.08 ± *0.00*	4.34 ± *0.00*	13.19 ± *0.00*	5.13 ± *0.00*	16.26 ± *0.00*	11.18 ± *0.00*	15.62 ± *0.00*	6.23 ± *0.00*	3.52 ± *0.00*	13.50 ± *0.00*	7.84 ± *0.00*
Clinopyroxene	0.00 ± *0.00*	0.00 ± *0.00*	0.00 ± *0.00*	0.00 ± *0.00*	0.00 ± *0.00*	0.00 ± *0.00*	0.00 ± *0.00*	0.00 ± *0.00*	0.00 ± *0.00*	0.00 ± *0.00*	0.00 ± *0.00*	0.00 ± *0.00*	0.00 ± *0.00*	0.00 ± *0.00*
Epidote	0.00 ± *0.00*	0.00 ± *0.00*	0.00 ± *0.00*	0.00 ± *0.00*	0.00 ± *0.00*	0.00 ± *0.00*	0.00 ± *0.00*	0.00 ± *0.00*	0.00 ± *0.00*	0.00 ± *0.00*	0.00 ± *0.00*	0.00 ± *0.00*	0.00 ± *0.00*	0.00 ± *0.00*
Garnet	0.00 ± *0.00*	0.00 ± *0.00*	0.00 ± *0.00*	0.00 ± *0.00*	1.18 ± *0.27*	0.00 ± *0.00*	1.21 ± *0.34*	0.00 ± *0.00*	0.00 ± *0.00*	0.28 ± *0.35*	0.16 ± *0.32*	0.00 ± *0.00*	0.00 ± *0.00*	0.00 ± *0.00*
Glass and Silica	18.67 ± *4.35*	18.44 ± *2.19*	8.33 ± *3.09*	15.22 ± *3.22*	20.12 ± *1.28*	13.90 ± *1.91*	13.09 ± *1.36*	22.86 ± *4.31*	13.51 ± *3.99*	26.52 ± *4.87*	41.53 ± *4.56*	0.95 ± *1.74*	3.02 ± *3.04*	10.71 ± *3.88*
Halide	0.00 ± *0.00*	1.83 ± *0.27*	3.56 ± *0.00*	1.32 ± *0.00*	1.71 ± *2.64*	0.00 ± *0.00*	1.64 ± *0.00*	2.60 ± *0.00*	2.14 ± *0.00*	2.08 ± *4.89*	3.29 ± *3.25*	3.37 ± *0.00*	2.20 ± *0.00*	0.85 ± *0.00*
K-Feldspar	0.00 ± *2.71*	0.00 ± *0.99*	0.00 ± *0.96*	0.00 ± *0.34*	1.97 ± *0.58*	0.00 ± *0.00*	0.00 ± *0.28*	0.00 ± *0.26*	0.00 ± *0.27*	0.00 ± *0.38*	0.61 ± *0.29*	0.00 ± *0.20*	0.00 ± *0.98*	0.00 ± *0.26*
Mica	3.91 ± *0.00*	12.07 ± *0.86*	10.06 ± *0.00*	3.25 ± ± *0.00*	0.00 ± *0.94*	5.62 ± *0.00*	0.00 ± *0.00*	12.33 ± *0.00*	11.47 ± *0.00*	2.57 ± *0.00*	0.00 ± *1.33*	0.00 ± *0.00*	5.27 ± *0.00*	4.04 ± *0.00*
Olivine	0.00 ± *0.00*	0.33 ± *0.00*	0.00 ± *0.80*	0.00 ± *2.73*	0.00 ± *0.00*	0.00 ± *0.56*	0.00 ± *0.00*	0.00 ± *1.09*	0.44 ± *1.13*	0.16 ± *3.37*	0.00 ± *0.00*	0.00 ± *0.00*	0.00 ± *0.97*	0.00 ± *0.98*
Orthopyroxene	0.00 ± *0.00*	0.00 ± *0.00*	4.87 ± *0.00*	9.35 ± *0.00*	0.00 ± *0.00*	0.00 ± *0.00*	0.00 ± *0.00*	0.00 ± *0.00*	0.00 ± *1.01*	0.00 ± *1.28*	0.00 ± *0.00*	0.00 ± *0.00*	0.00 ± *0.00*	0.00 ± *0.00*
Oxide	6.16 ± *1.48*	0.00 ± *0.00*	6.03 ± *3.26*	9.41 ± *3.72*	8.78 ± *0.00*	8.32 ± *0.00*	6.52 ± *0.00*	4.89 ± *0.00*	4.30 ± *0.00*	8.81 ± *0.00*	7.76 ± *0.00*	0.00 ± *0.00*	0.68 ± *0.00*	0.26 ± *0.00*
Phosphate	2.75 ± *1.93*	1.58 ± *1.36*	0.01 ± *0.92*	1.50 ± *1.33*	0.00 ± *0.91*	0.00 ± *0.59*	0.00 ± *0.66*	0.03 ± *1.39*	0.72 ± *1.48*	0.00 ± *1.69*	0.00 ± *0.79*	6.31 ± *0.00*	0.81 ± *0.83*	1.74 ± *0.33*
Plagioclase	24.40 ± *1.91*	15.15 ± *1.74*	24.29 ± *2.10*	21.26 ± *1.84*	45.17 ± *0.00*	16.25 ± *0.00*	51.01 ± *0.00*	10.83 ± *0.88*	7.10 ± *0.99*	20.21 ± *0.00*	34.74 ± *0.00*	12.64 ± *0.98*	28.67 ± *0.30*	13.44 ± *0.71*
Quartz	22.89 ± *0.72*	23.53 ± *0.63*	17.90 ± *2.07*	14.84 ± *2.38*	12.17 ± *1.61*	29.25 ± *1.28*	12.30 ± *1.62*	15.98 ± *0.78*	29.41 ± *2.09*	9.02 ± *3.03*	2.27 ± *2.11*	18.17 ± *0.60*	33.45 ± *1.36*	47.69 ± *1.76*
Serpentine	0.00 ± *0.00*	0.00 ± *0.00*	0.00 ± *0.64*	0.00 ± *0.61*	0.00 ± *0.45*	0.00 ± *0.52*	0.00 ± *0.57*	0.00 ± *0.66*	0.00 ± *0.70*	0.00 ± *0.64*	0.00 ± *0.41*	0.00 ± *0.54*	0.00 ± *0.65*	0.00 ± *0.55*
Sulfate	0.12 ± *1.13*	0.84 ± *0.95*	0.70 ± *0.79*	0.84 ± *0.94*	0.00 ± *0.00*	0.00 ± *0.00*	0.00 ± *0.00*	0.00 ± *0.00*	0.00 ± *0.00*	0.00 ± *0.00*	0.00 ± *0.00*	6.30 ± *1.08*	0.00 ± *0.00*	0.32 ± *0.92*
Zeolite	0.00 ± *0.00*	0.00 ± *0.00*	0.00 ± *0.00*	0.00 ± *0.00*	0.00 ± *0.00*	0.00 ± *0.00*	0.00 ± *0.00*	0.00 ± *0.00*	0.00 ± *0.00*	0.00 ± *0.00*	0.00 ± *0.00*	0.00 ± *0.00*	0.00 ± *0.00*	0.00 ± *0.00*

[a]Statistical errors from the NNLS are italicized below mineral group abundances [*Rogers and Aharonson*, 2008].
[b]Silica and glass abundances are grouped together due to their remarkably similar spectral shapes [*Glotch et al.*, 2006].

spectra is due to the high abundance of quartz. However, there is a variation in the shape of these absorptions (ranging from rounded to pointed), which is characteristic of differences between macrocrystalline and microcrystalline quartz [*Hardgrove and Rogers*, 2014]. Conversely, the common quartz doublet is less prominent in mudstones, except for sample *SM-75-117*. Also observed in the same spectral region, but sample dependent, are notable deviations from the typical quartz doublet, which can be influenced by contributions from sheet silicate, sulfate, or plagioclase phases. Feldspar spectral features are present in the ~1300–950 cm^{-1} range, consistent with the significant abundances of feldspar in the sandstone and mudstone samples. Lastly, deep carbonate absorption features are present in the ~1550–1450 cm^{-1} region for some samples. The shape of these features is most consistent with dolomite.

4.1.1. Sandstone TIR Models

Table 3 lists the modeled results for bulk mineralogy, as determined from the unmixing of TIR spectra (section 3.2.2), and Figure 2 shows the model fits for each rock spectrum. On average, sandstone models identified between 8 and 9 mineral phases per sample. Quartz was modeled in every sandstone sample, with abundances ranging from ~21 to 77 vol % and an average of ~52 vol %. After quartz, the most abundant mineral groups used in the models are clays and plagioclase. Albite was the most frequently identified plagioclase phase, but other feldspars, including bytownite, oligoclase, and anorthite, are also detected. For clays, smectite group members, in particular Beidellite SBCa-1, are the most frequently modeled mineral phases. Carbonates, phosphates, and sulfates are commonly modeled for sandstone samples, with abundances usually below ~7.5 vol %. One sample, *Gratton*, exhibits a modeled carbonate abundance of 42%.

Although spectral differences between the bulk rock and the model fits are generally small, there are noticeable areas of misfit that can be generalized into two wave number groups between ~1150–1250 cm^{-1} and ~500–600 cm^{-1} (Figure 2). Mineral groups most likely linked to these model misfits

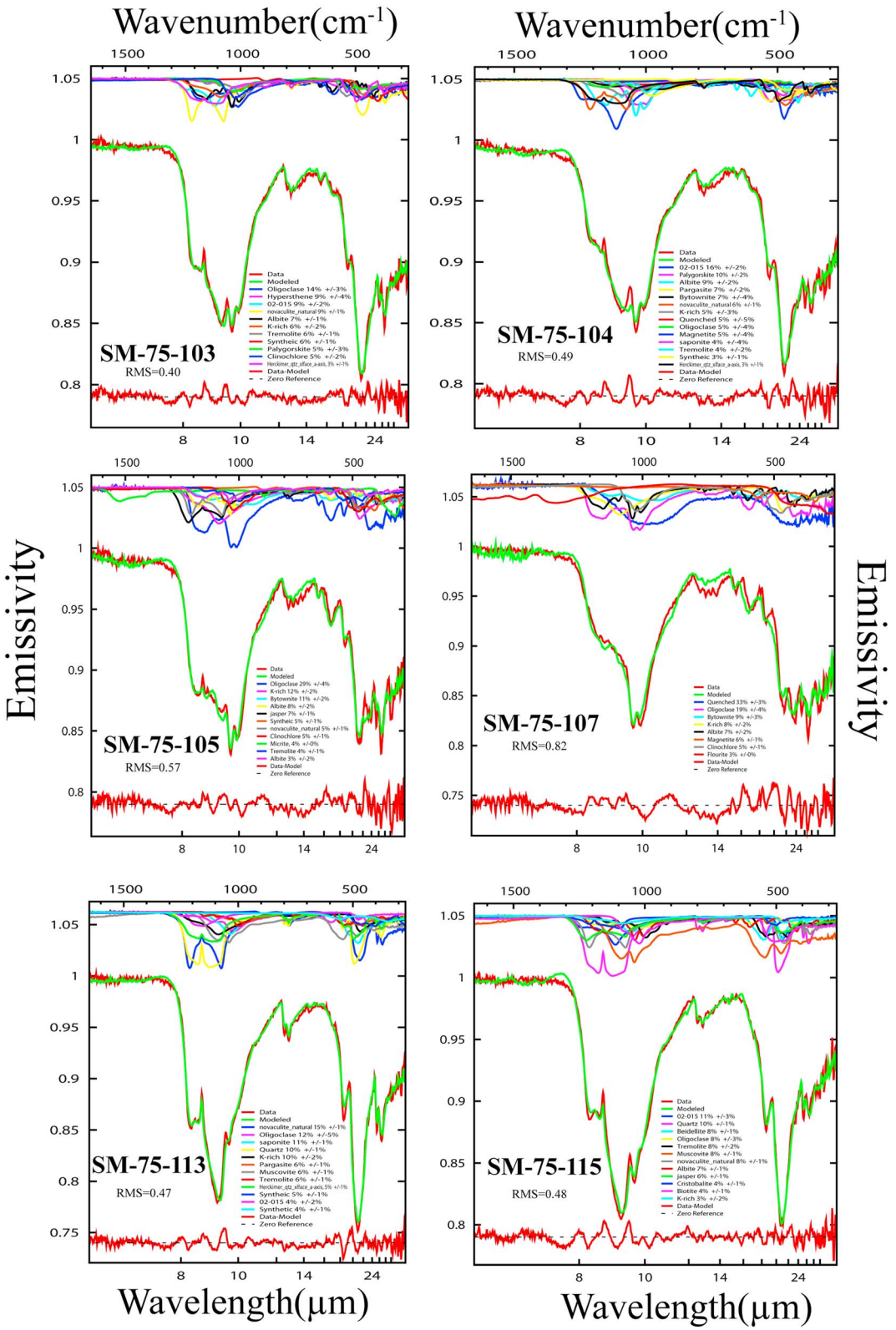

Figure 3. Measured versus modeled TIR emission spectra of 14 mudstones. Only individual mineral phases with abundances ≥ 3 vol % are displayed. In general, RMS values indicate a good fit between the measured and modeled spectra. Any deviation from a one-to-one relationship is highlighted using a zero reference line.

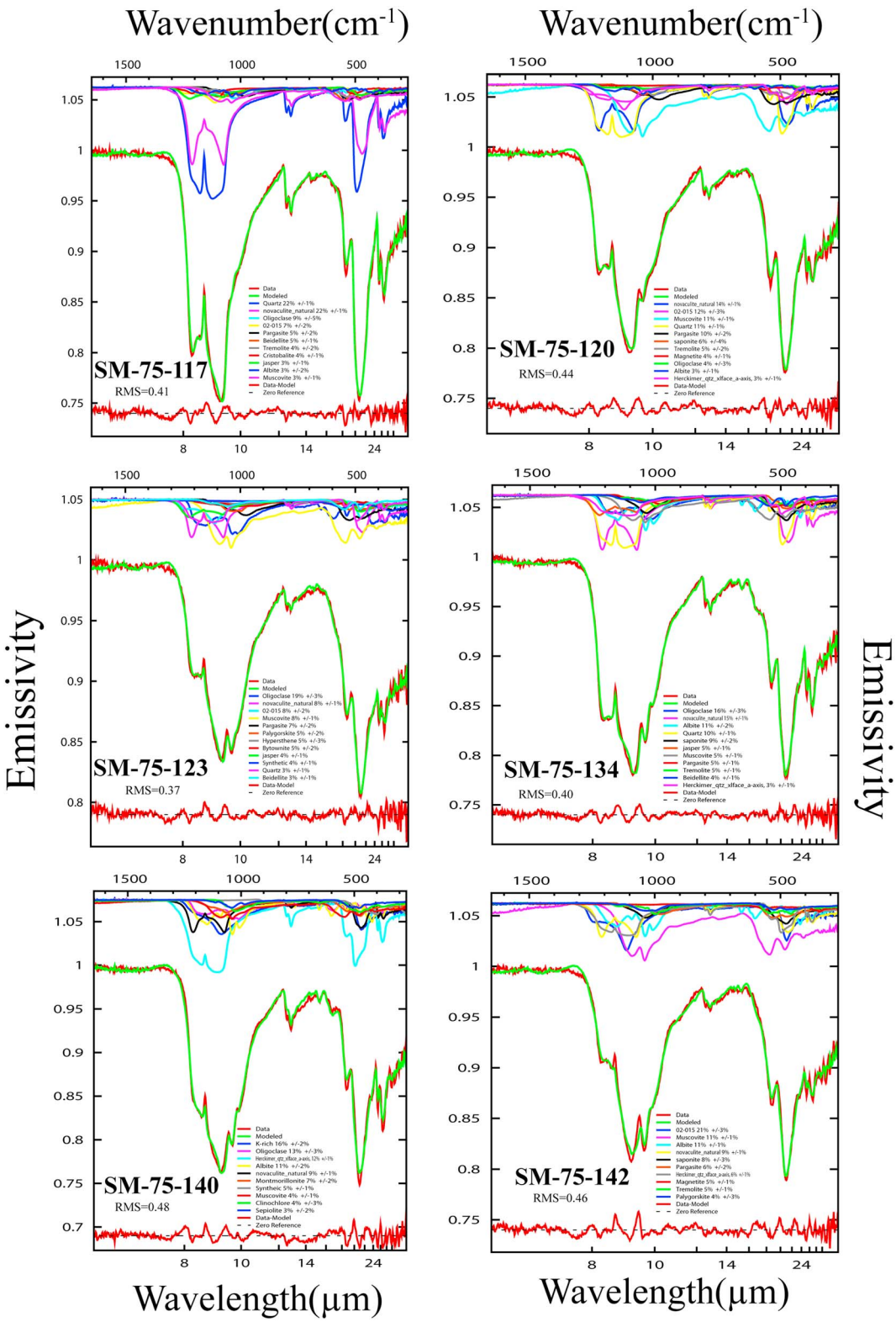

Figure 3. (continued)

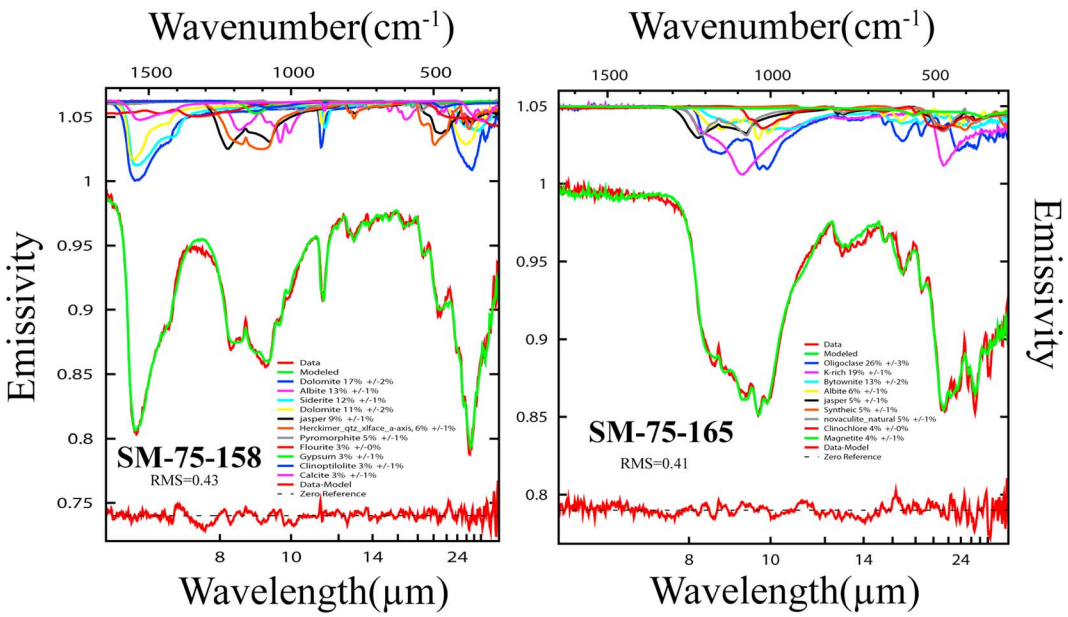

Figure 3. (continued)

are the micas and clays within the sandstones' matrix. Further discussion of the influence these minerals phases have on TIR spectra as well as the potential reasons for model inconsistency are addressed in sections 5.1 and 5.2.

4.1.2. Mudstone TIR Models

Table 4 lists the modeled results for bulk mineralogy of the mudstone samples, as determined from the unmixing of TIR spectra (section 3.2.2), and Figure 3 shows the model fits for each rock spectrum. On average, between 10 and 11 mineral phases are used to fit each mudstone spectrum. Plagioclase is modeled with the highest average abundance of ~23 vol % and is used in every mudstone spectral model. Mineral abundances and individual phases are sample dependent, but, in general, two plagioclase solid solution members, Albite WAR-0612 and Oligoclase BUR-060 are commonly identified. Clays, glass, and quartz are the next most frequently used mineral groups, with modeled abundances between ~10 and 21 vol %. Microcrystalline quartz is the more commonly identified quartz phase, whereas the chlorite group member, clinochlore, is the most commonly modeled sheet silicate. Glass phases, mainly a SiO-K glass similar to obsidian (listed as "K-rich glass" in Figures 2 and 3), is used in all of the unmixing models and accounted for an average abundance of ~13 vol %. Mica, specifically muscovite, accounted for an average abundance of ~5 vol % and is used in 70% of the models. Oxide, amphibole, and carbonate phases are commonly used in the model fits and collectively accounted for an average abundance of ~20 vol %.

As with sandstones, differences between the measured and modeled spectra are generally low (Figure 3). Overall, there are only subtle misfits between the bulk rock spectra and the modeled spectra, with a RMS average of 0.48, comparable to sandstone models, which have an RMS average of 0.50. However, the range of RMS values between 0.37 and 0.82 indicates a higher degree of misfit between select mudstones models when compared to the sandstone models, which have an RMS range of 0.25 to 0.69. Model inconsistencies are most apparent in the ~1100–1300 cm^{-1} region and are commonly associated with mica contributions. This is addressed further in section 5.

4.2. Sandstone Point Counts

Modal mineralogy determined from point counts is shown in Table 5. We broke mineral identification down into six classes: quartz, plagioclase feldspar, potassium feldspar (Kspar), micas, "lithic plus," and matrix minerals. The first four mineral classes are considered the primary detrital minerals, and the optical identification of these minerals is straightforward with the use of a petrologic microscope. Traditionally, grains counted as lithic fragments consist of any polymineralic pieces of a preexisting rock that has weathered down to a

Table 5. Sandstone Mineral Abundances Determined From Traditional Point Counts[a]

	Gratton	Mt. Tom	Flat Irons	Berea	Smithwick	Devil K	16-606	La Boca	Catskill Sk-1	Mis-Te-2	Tx-Te-1	D1-72-92	Carapace
Quartz	48	47	51	66	71	73	56	45	64	58	52	55	42
Plagioclase	16	29	3	0	1	0	2	12	6	0	3	9	4
Kspar	0	7	27	0	1	0	0	1	6	2	8	17	2
Micas	3	2	2	2	1	0	4	7	1	3	3	0	3
Lithics Plus	3	2	0	0	0	1	2	4	0	2	5	0	6
Matrix	29	13	17	31	26	25	35	31	23	35	29	18	43
Matrix Components	Chlorite, rock flour matrix	Iron-rich clay	Micaceous clay	Micaceous clay	Clay matrix	Chlorite, carbonate, and quartz	Clay matrix	Clay matrix	Calcite cement	Hematite cement	Clay matrix	Calcite cement	Zeolite cement with minor calcite

[a]Error quoted for traditional point counts of 250 points results in <6% absolute error [*Van Der Plas and Tobi*, 1965].

sand-sized grain and incorporated into the sandstone rock [*Blatt et al.*, 2006]. In these cases, the lithic fragment compositions are qualitatively assessed because the origin of preexisting rock can give substantial insight to provenance. However, in this work, a "lithic plus" group was created to include lithic fragments, oxides, and accessory minerals, due to the minor volume percentage each group member accounted for. Although this presents some ambiguity for direct comparison to TIR spectral models, this group accounts for <5% of counted grains, and this should not have a significant impact on the comparisons. Lastly, our matrix class consisted of any mineral grains that were smaller than 30 μm and filled the interstitial spaces between the primary detrital minerals of the first four classes, including matrix grains and cement. The matrix group was created to incorporate all fine-grained material below the detection capability of a petrologic microscope. This group was also qualitatively assessed based upon distinguishing optical features and generalized components, which are listed in Table 5. Common matrix components consist of multiple clay phases, finely grained micas, quartz, hematite, and calcite. The sandstone matrix assessed solely from point counting procedures presents a major source of ambiguity when comparing quantitative individual mineral abundances with TIR-derived abundances. For example, TIR spectra would be sensitive to both detrital grain quartz and matrix quartz, but point counting yields an estimate of only detrital quartz. This is discussed further in sections 4.4 and 6.

4.3. Quantitative XRD

Mineralogy determined from whole-pattern fitting of mudstone XRD patterns serves as the "known" abundances, in which TIR modeled mineral volume percentages are compared (Table 6). Quantitative XRD (QXRD) abundances are converted from weight percentages into volume percentages in order to be directly comparable to modeled results (Table 6). Plagioclase, mainly albite, and muscovite are the dominant mineral abundances identified from XRD pattern refinements. Also, chlorite is commonly observed in almost all of our mudstone samples (Table 6). These XRD abundances are consistent with the normative analysis presented in *McLennan et al.* [1979].

4.4. Bulk Mineralogy (Known Versus Modeled)

Modal mineralogy determined from petrologic point counts (known) is compared with spectrally derived (modeled) abundances for each sandstone, whereas XRD abundances serve as the known for mudstone comparisons. Figures 4 and 5 show a comparison between TIR- and point count-derived or XRD-derived abundances for total quartz and total feldspar, the dominant phases. Similarly, Figures 6 and 7 display a comparison between techniques for all other mineral abundances. The "total other" class includes what is interpreted as the matrix determined by traditional point counts (~ <30 μm), and in this case represents mainly the sheet-silicate contributions, as determined by visual assessment. This generalization for TIR mineral abundances may inherently result in incorrect estimation of mineral phases, because

Table 6. Mudstone Mineral Volume Abundances Determined by Full Pattern X-ray Diffraction Quantitative Refinements[a,b]

	SM-75-123	SM-75-117	SM-75-115	SM-75-142	SM-75-120	SM-75-113	SM-75-158	SM-75-140	SM-75-134	SM-75-107	SM-75-105	SM-75-104	SM-75-103	SM-75-165
Plagioclase	28.37	15.38	10.90	8.28	7.35	12.39	16.84	22.85	24.08	40.22	45.78	19.44	25.23	39.35
Kspar	0.00	0.00	0.00	0.00	0.26	0.00	0.00	1.00	0.00	12.08	0.00	0.00	0.00	12.90
Quartz	25.64	45.99	29.97	27.35	37.86	38.01	65.41	40.37	34.74	14.67	20.97	22.91	21.12	17.48
Clay	7.76	16.99	15.06	14.90	15.32	5.74	3.20	4.17	10.39	23.87	19.64	14.92	17.16	21.02
Oxide	0.20	0.00	0.00	0.00	0.08	0.00	0.00	0.00	0.05	0.14	0.09	0.82	0.32	0.02
Mica	37.97	21.04	43.35	49.08	38.56	43.29	14.30	30.82	29.80	6.30	10.91	41.02	35.17	7.24
Carbonate	0.00	0.00	0.00	0.00	0.00	0.00	0.00	0.65	0.41	1.27	1.24	0.00	0.00	0.50
Sulfide	0.06	0.00	0.00	0.00	0.00	0.06	0.00	0.00	0.02	0.15	0.07	0.00	0.00	0.00
Neosilicate	0.00	0.60	0.72	0.39	0.57	0.50	0.25	0.14	0.51	1.31	1.31	0.89	1.00	1.49

[a]Refinement uncertainties for major crystalline phases are generally <5 vol % [*Środon et al.*, 2001].
[b]Weight abundances were converted to volume abundances in order to be directly comparable to the other techniques used in this investigation.

the matrix may also include other clay-sized mineral phases (including quartz and feldspar). However, this allows for a first-order comparison of bulk mineralogy results. Also grouped together in Figures 6 and 7 are modeled silica and glass phases, due to their similar spectral shapes [*Glotch et al.*, 2006]. Lastly, traditional point count abundances for the lithic plus group are compared with TIR oxide derived abundances. In the lithic plus group, iron- and titanium-rich oxides account for the majority of grains visually identified by point counts, making a comparison of this group to the TIR oxide abundances a reasonable assumption. However, in this investigation we recognize that there is no perfect comparison across techniques for evaluating sand-sized lithic fragments of potentially varying parent lithology (e.g., plutonic versus metamorphic fragments). Furthermore, sand-sized grains of comminuted source rock may be composed of intergrown igneous crystals or conversely foliated minerals, thus making individual abundances indiscernible by traditional point counts.

Mineral abundances determined from thermal emission data, XRD refinements, and petrologic point counts are in good agreement, based on a linear comparison of abundances falling within a 15 vol % threshold. For sandstones, quartz displays the lowest mean difference of 6.0 vol % (Table 7 and Figures 4 and 5). Both feldspar and total other also display strong correlations but with slightly higher average absolute differences of 7.2 vol % and 14.8 vol %, respectively. These sandstone absolute differences and uncertainties fall within the accuracy associated with traditional point counting techniques, which also compares well with previous bulk rock TIR models [*Feely and Christensen*, 1999; *Hamilton and Christensen*, 2000; and *Wyatt et al.*, 2001]. However, individual components making up the total other class display significant inconsistencies between techniques. Specifically, the largest deviations from a linear mixing model are displayed in abundances for sheet silicates and the matrix determined by point counts, carbonates, and a glass/silica group (Figure 7).

In comparison, for mudstones, feldspar displays the lowest average absolute difference between the measured and modeled abundances (4.2 vol %) (Table 7). Quartz and total other exhibit slightly higher mean differences (11.2 and 12.5 vol %, respectively) but are also still well within model agreements determined from the previous studies of igneous and metamorphic rocks [*Feely and Christensen*, 1999]. Similar to sandstones, mudstone abundances for total other components deviate considerably when compared across techniques. The largest discrepancy is displayed in comparing micas, carbonates, and a glass/silica group.

Despite the issues previously described, the majority of rock samples can still be placed into common classification schemes used for clastic sedimentary compositional analysis. For example, comparing the abundances of quartz,

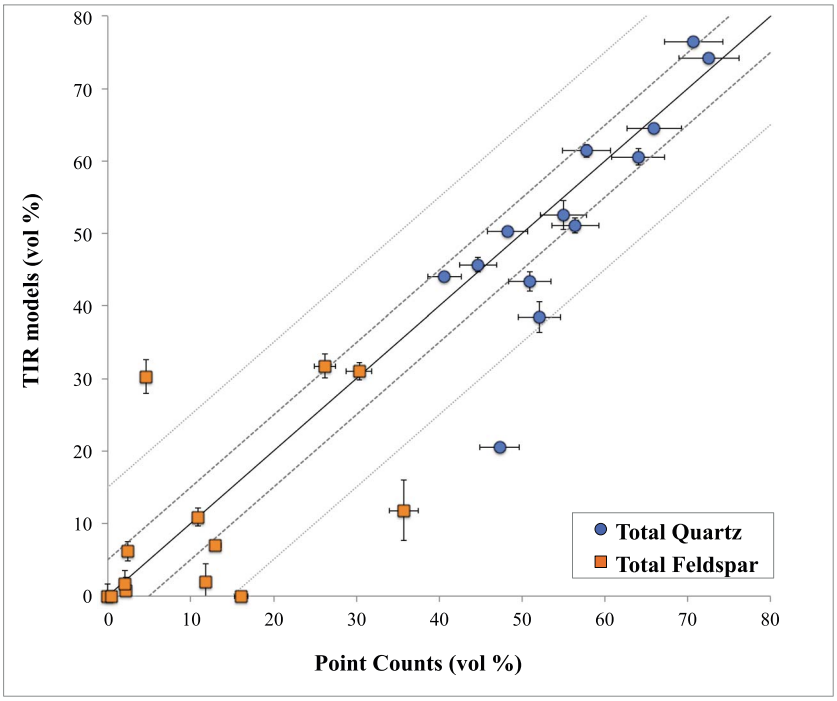

Figure 4. A scatterplot of the quartz and feldspar mineral volume abundances for sandstones determined from traditional point counts versus modeled mineral abundances derived from unmixing TIR spectra displays an extremely good fit. The solid line indicates a one-to-one relationship between the models, whereas, the lighter dotted lines represent a boundary of ±5 vol % and ±15 vol %. A relatively linear mixing correlation between the two techniques can be concluded from this plot. Technique uncertainties are displayed by the error bars and are unique to each sample for TIR models (Table 3) and are averaged for point counts at 5 vol % (section 3.2.6).

feldspar, and all other minerals allows for ~62% TIR sandstone model abundances to be classified in the same respective field as point count abundances (Figure 8), with minor discrepancies potentially caused by errors associated with each technique. Furthermore, adding mudstones to the same ternary plot and creating a 50% total "other" abundance boundary creates a sufficient way to appropriately classify ~57% of mudstones and ~85% of sandstones (Figure 9).Comparing mudstone classifications between XRD and TIR abundances demonstrates a correlation between the two measurement techniques, but TIR models correctly classify ~71% of mudstones, whereas XRD results only place ~43% samples as mudstones.

5. Discussion

In general, thermal emission spectral models produce results consistent with other commonly used techniques for quantifying mineral abundances of mudstones and sandstones (Figures 4–7). Below, we further discuss the effectiveness of TIR spectroscopy at identifying individual mineral phases as well as the usefulness of TIR spectroscopy at classifying the bulk mineralogy of sand-sized or smaller-grained sedimentary rocks. We also discuss limitations with all techniques used here and possible reasons for differing abundance estimates in some samples.

5.1. Quartz and Feldspar Abundances

Sedimentary primary minerals, mainly detrital quartz and feldspar grains, display similar abundances between TIR models and their coanalyzed techniques. Quartz and feldspar exhibit high volume abundances, accounting for ~65% and ~50% of total mineral abundances in sandstones and mudstones, respectively. For sandstones, quartz dominates the mineral abundances and deviates from the traditional point counts by ~6 ± 7% (Table 7). In comparison, for mudstones, quartz is systematically underestimated in TIR models (but still within 11 ± 11% of the known). This is addressed further in section 5.3.

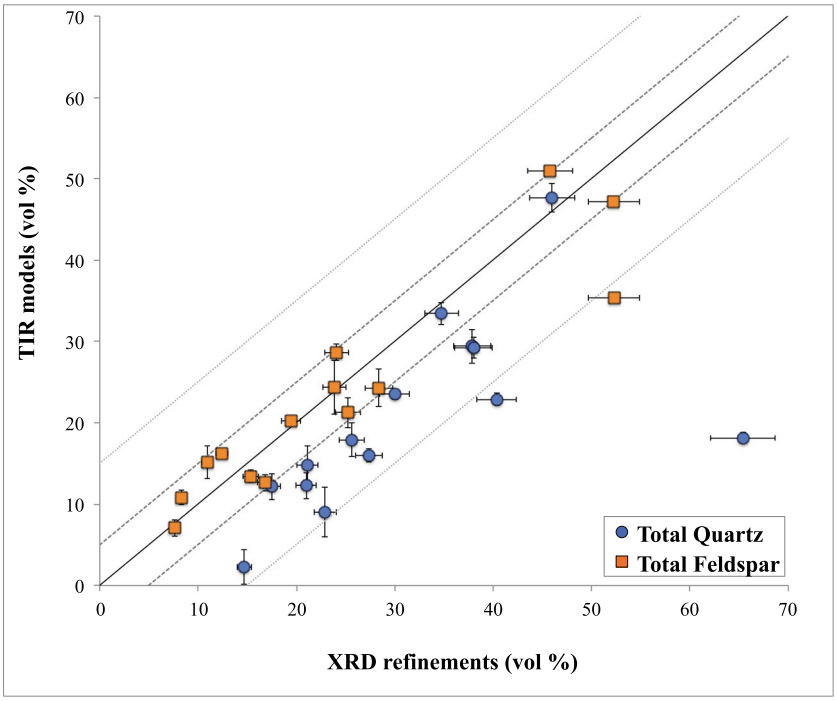

Figure 5. A scatterplot of mineral volume abundances for mudstones determined from full pattern X-ray diffraction quantitative refinements versus modeled TIR abundances. Similar to sandstones, mudstones display an extremely good fit. The three boundaries consist of a perfect fit (solid line), a ±5 vol % difference (darker dotted line), and a ±15 vol % (lighter dotted line). TIR technique uncertainties are displayed by the error bars and are unique to each sample (Table 4) and averaged at 5 vol % for XRD abundances (section 3.2.6).

Feldspars in sedimentary rocks can be diagenetically altered (e.g., surface weathering and low grade metamorphism), thus making identification by various techniques a challenging task. However, comparison among techniques for the two different sedimentary rock grain sizes display similar results, consistent with the previous assessment of TIR capability in identifying feldspars of known compositions within 4 vol % accuracy [*Hecker et al.*, 2010]. Based on the microstructures (i.e., polysynthetic twinning) of feldspars in sandstone thin sections that were optically observed, feldspar identification across traditional point counts is in agreement with TIR derived phases. Plagioclase, mainly albite and oligoclase, is the most frequently modeled feldspar in the TIR spectra of mudstones, showing consistency with QXRD-derived abundances. Additionally, previous geochemical and petrographic analyses of the Huronian mudstones used in this study suggest that sodium metasomatism (e.g., albitization) was widespread in this formation [*Fedo et al.*, 1997]. Although the TIR and QXRD results do not suggest complete albitization, the evidence for the transformation between end-members in the *An-Ab* solid solution series is clearly present in both bulk analytical techniques used to classify these mudstone samples.

For sandstones, modeled feldspar abundances are accurate to within 7 ± 9%, with a few outlier points driving the large standard deviations (Figure 4). One possible reason for this discrepancy can be the difficulty for both techniques in discerning between diagenetically altered feldspar and clay. Traditional point counts may have noted a degree of alteration along the rim of a feldspar grain and still classified the grain as feldspar, whereas TIR spectroscopy with a sample penetrating depth on the order of ~10^0–10^1 μm may have acquired spectral features of sheet silicates, resulting in disproportional abundances in the TIR spectra.

5.2. All Other Minerals

For sandstones, all other minerals combined comprise approximately one third of the total volume abundances, whereas in mudstones the total other mineral class accounted for about half of the bulk rock abundances. Total other abundances for sandstones display an average difference of 14.8 ± 14.6 vol % from the known, and for mudstones an average difference of 12.5 ± 13.4 vol % from the known (Table 7). Grouping

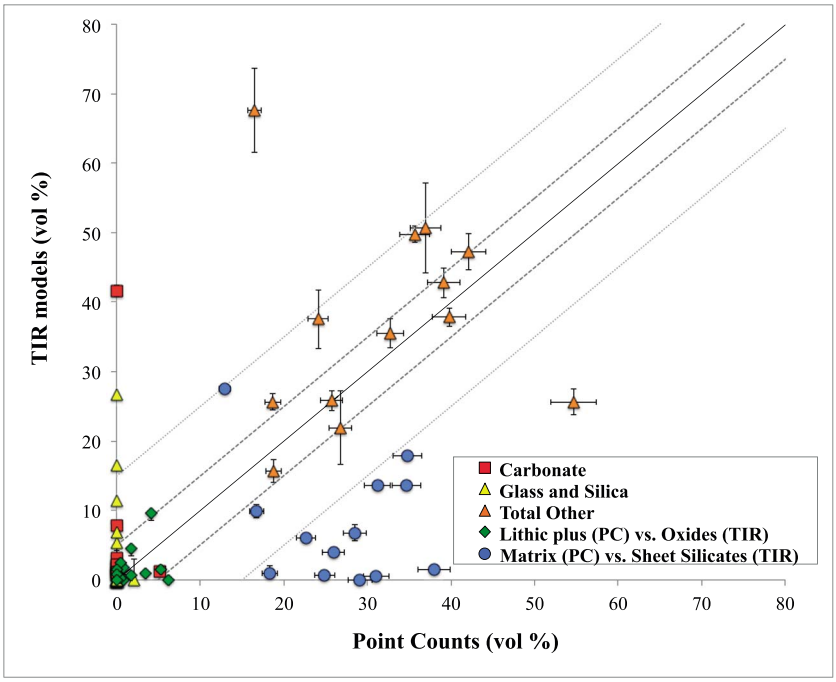

Figure 6. All other sandstone mineral volume abundances for TIR models and point counts (PC) are compared. A one-to-one correlation is shown by the solid line with 5% and 15% difference envelopes displayed in the lighter dotted lines. Matrix abundances determined by point counts are plotted against TIR sheet silicate abundances. The total other class displays accuracies within 15 vol %, demonstrating the ability of TIR to constrain volume abundances. The underestimation of sheet-silicate volume abundances suggests that either there are additional phases present in the clay-sized fraction of sandstones or that nonlinear spectral mixing is occurring (section 5**).** Error bars associated with each point are dependent on technique uncertainness, described further in section 3.2.6.

all other minerals together allows for an assessment of the traditional bulk rock classification, which is dependent on accurate determination of the relative proportions of detrital grains and matrix (i.e., arenites, wackes, or mudstones) **(**Figure 9). However, in order to more clearly understand TIR model accuracy, below we compare derived abundances for individual mineral groups within the total other category, for each technique.

5.2.1. Sheet Silicates

For sandstones, if it is assumed that the matrix abundances determined from traditional point counts are dominated by sheet silicates, then Figure 6 indicates that TIR models underestimate sheet-silicate abundances. Furthermore, TIR models predict a large component of amorphous silica ("glass + silica"), which are not likely to be present in these rocks at such high abundances. This discrepancy may arise for one or more reasons: (1) the matrix components may not be entirely composed of sheet silicates and may include clay-sized quartz, feldspar, carbonate, or other phases and/or (2) nonlinear spectral mixing is occurring in the matrix (section 5.3), which is the finest grain size fraction of the sandstones.

Additional insight into sheet-silicate discrepancies comes from the mudstone analyses (Figure 7), where minerals that comprise the total other group are more easily compared because TIR and XRD are both bulk techniques that are not restricted to optical identification. In the mudstones, we can see that among sheet-silicate phases, it is mica that is most commonly underestimated, whereas clay minerals are more accurately predicted. The low-modeled abundances of mica appear to be largely offset by high modeled abundances of amorphous silica (glass + silica), as well as carbonates in a few cases. However, the mudstones used for this investigation are unlikely to contain poorly crystalline material, which is further supported by XRD patterns displaying no indication of X-ray amorphous phases.

The underestimation of mica for sandstones and mudstones from TIR models may partially arise from the crystal form of micas. Specifically, muscovite and the fine-grained counterpart sericite tend to have platy-like crystals due to their perfect basal cleavage, and result in flakes of mica with the thickness of grains much less

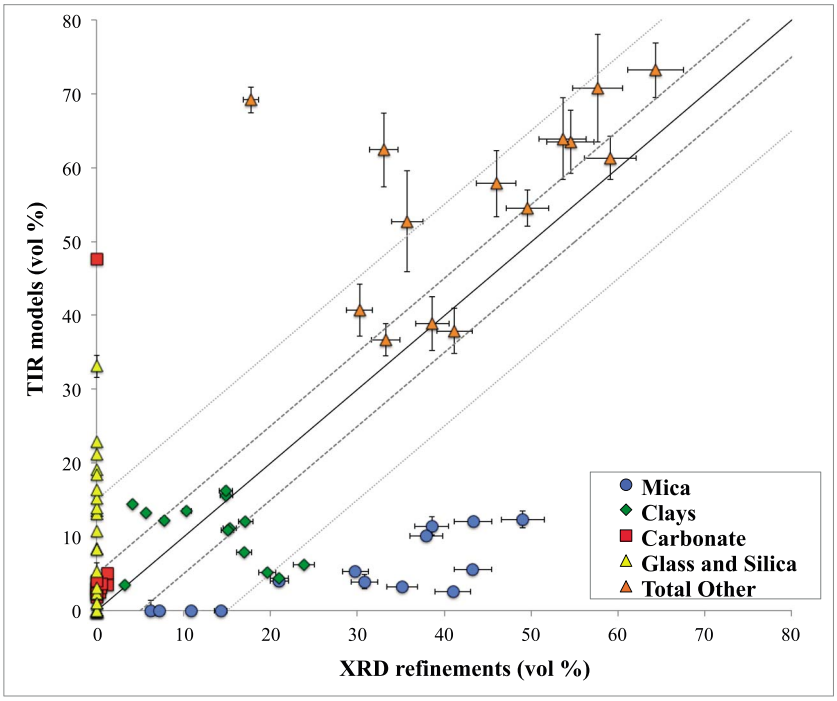

Figure 7. XRD and TIR abundances for all other minerals are plotted to identify key misfits between the two techniques. TIR models generally highly underestimate mica abundances and highly overestimate carbonates and a silica/glass group. The sum of all other mineral abundances into a total other group displays significant correlation with accuracies within 12.5 vol %. Similar to previous scatterplots, a perfect fit (solid line), 5% boundary (darker dotted line), and a 15% boundary (lighter dotted line) are displayed to evaluate agreement across techniques. Technique uncertainties (section 3.2.6) are displayed as error bars for each point and are recorded in Table 4.

than the length and width dimensions. This may result in emitted photons penetrating though the optically transparent grain and interacting with multiple phases (section 5.3).

Clay minerals are modeled within 7.1 ± 5.8 vol % of the known but display no systematic overestimation or underestimation when comparing TIR and XRD abundances. Generally, XRD results determined that chlorite group members are the dominant clay phases present in the Huronian mudstones. These results coincide with TIR models, which commonly identified clinochlore, a tri-octahedral chlorite group member, as one of the clay phases present. However, TIR models also commonly identified palygorskite, a smectite group member, which is inconsistent with the XRD results. Furthermore, these ancient mudstones (2.5 Ga) have experienced low-grade metamorphism and are thus unlikely to contain pure smectites. This is consistent with

Table 7. Comparison Between the TIR, Point Count, and XRD Derived Mineral Abundances[a]

	Sandstone Mean ± 1 σ Difference (%)[b]	Mudstone Mean ± 1 σ Difference (%)[b]	Sandstone Median Difference (%)[b]	Mudstone Median Difference (%)[b]
Quartz	6.0 ± 7.1	11.2 ± 11.3	3.5	8.6
Feldspar	7.2 ± 9.1	4.2 ± 4.0	3.7	4.0
Other	14.8 ± 14.6	12.5 ± 13.4	11.3	9.6
Mica[c]	-	24.2 ± 11.1	-	27.0
Clay	-	7.1 ± 5.8	-	4.8
Carbonate	-	5.9 ± 12.0	-	2.7

[a]Mean differences are calculated from the absolute differences in mineral abundances, shown in Figures 5 and 6.
[b]Uncertainties listed for the differences are the standard deviation of the absolute values of the difference between measured and modeled abundances.
[c]Subgroups for mudstone comparisons are italicized. There is no direct comparison for matrix abundances between sandstone point counts and TIR models.

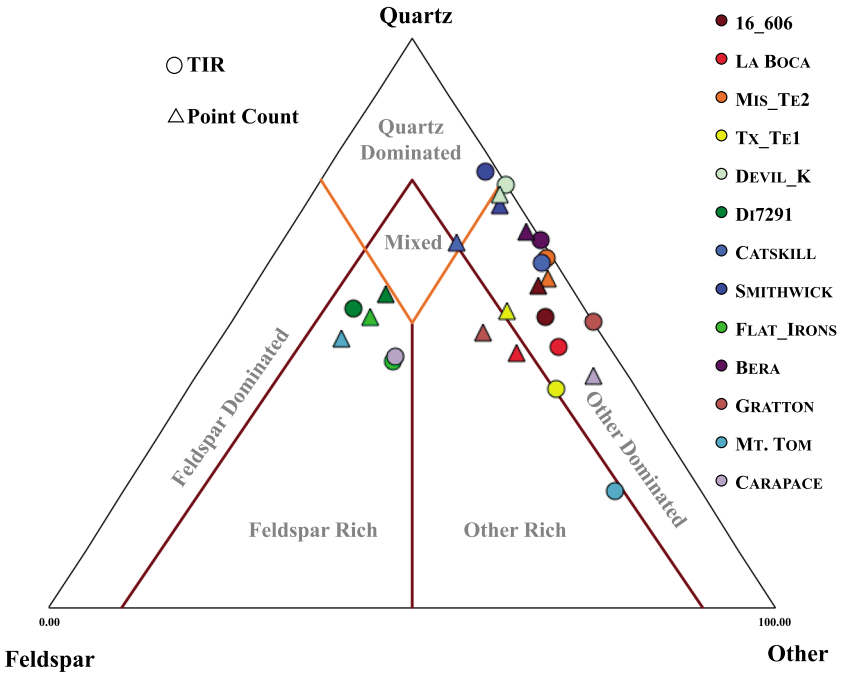

Figure 8. A classic sandstone classification [*Dott*, 1964] is modified to accommodate TIR models by changing the rock fragment apex to total other, which includes all other mineral phases. For the sandstones analyzed, ~62% of the rocks would be placed in the same respective class as point count classification.

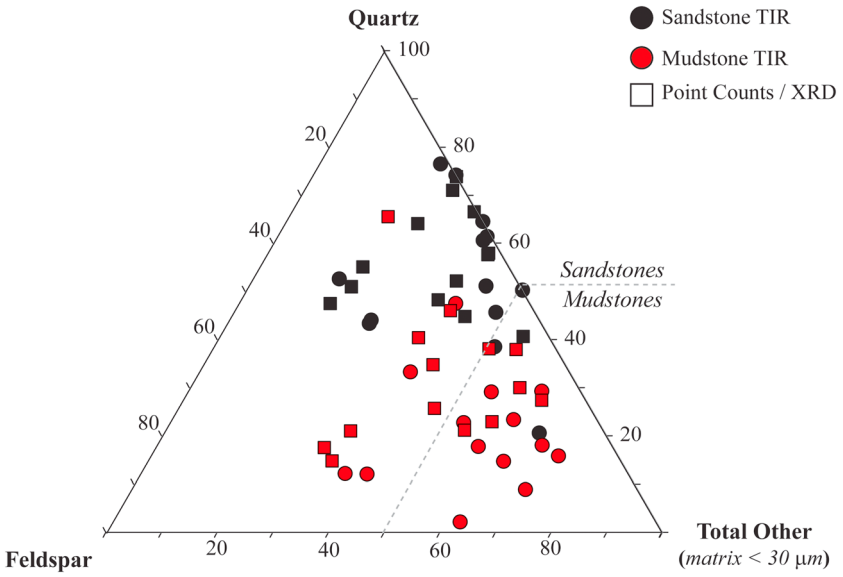

Figure 9. A similar ternary plot as seen in Figure 8, except now mudstones and sandstones are plotted together. A join line (marked by the dotted gray line) creates a boundary of samples containing at least 50% of our total other class, which includes the most likely mineral phases contributing to the matrix abundances. This join line was based on the speculated average composition of mudstones, consisting 50 % clay minerals or fines, 30 % quartz and 10 % feldspar [*Boggs*, 1987]. This ternary diagram demonstrates the ability of TIR at discerning between clastic rock types, with ~57% of mudstones and ~85% of sandstones correctly identified. XRD abundances show a correlation with TIR mudstone abundances; however, ~71% of TIR models correctly classified, whereas only ~43% of XRD appropriately identified the samples as mudstones.

previous work by *Michalski et al.* [2006], where TIR models led to accurate clay abundance estimates, but the species of clay was commonly misidentified.

5.2.2. Carbonates

TIR spectra for three mudstones and two sandstones display an obvious carbonate contribution determined from absorptions present in the frequency range of ~1600–1500 cm^{-1} and ~850–900 cm^{-1} (Figure 1); however, for these same examples, traditional point counts and XRD refinements do not detect significant carbonate abundances. Overestimates of carbonate abundance in controlled mixtures were also commonly observed in companion paper 2. Thus, a finding is that thermal emission spectroscopy is highly sensitive to carbonates when mixed with silicates (section 5.3). Conversely, this sensitivity may also result in TIR modeled abundances for carbonates that are overestimated.

5.3. Causes for Discrepancies Between Methods

Discrepancies in mudstone mineral abundances and sandstone matrix abundances between techniques are likely largely due to the small grain sizes of these materials. With decreasing grain size, the grains become optically thin over portions of the TIR wavelength range [e.g., *Hunt and Logan*, 1972], which would result in the grain being transparent at those wavelengths. This allows emitted photons to interact with multiple mineral phases, which can result in nonlinear spectral mixing behavior [*Salisbury and Wald*, 1992; *Ramsey and Christensen*, 1998]. Spectral measurements on controlled fine-grained mineral mixtures, compacted in pellet form, clearly demonstrate the effects of nonlinear mixing in solids (paper 2, *Pan et al.* [2015].

Based on this work and results presented in paper 2, and relying on theory presented or summarized in previous work [e.g., *Vincent and Hunt*, 1968; *Hunt and Logan*, 1972; *Salisbury and Wald*, 1992; *Moersch and Christensen*, 1995], we suggest that the degree to which this effect occurs in fine-grained mixtures depends greatly on what phases are in the mixture. Specifically, it depends on where the spectral regions of strongest and weakest absorption are located for each component and the overall magnitude of the absorption coefficient (k) for the most strongly absorbing wavelength regions. For a mixture of components with small, uniform grain sizes, if the strongly absorbing wavelength regions for each component roughly coincide, and if the weakly absorbing wavelength regions coincide, then multiple photon interactions should be minimized and component spectra would combine linearly in those wavelength regions. Similarly, where weakly absorbing wavelength regions roughly coincide, there would be little absorption from any component, resulting in near-unit emissivity in those regions. For the opposite case, where strongly and weakly absorbing wavelength regions are different for each component, nonlinear spectral mixing would be greatly enhanced. An example of this would be the carbonate-bearing mixtures discussed in section 5.2.2. One of the two strongest carbonate absorptions (located between ~1450 and 1600 cm^{-1}) is located in a wavelength region where silicates are very weakly absorbing. The weakly absorbing nature of the silicates allows the carbonate feature to remain pronounced despite low abundance in the mixture. This also may explain why model accuracy for fine-grained igneous rocks, whose spectral mixing behavior was characterized in previous studies [*Feely and Christensen*, 1999; *Hamilton and Christensen*, 2000; *Wyatt et al.*, 2001], is similar to that for coarse grained sands [*Ramsey and Christensen*, 1998]. The major components of those rocks (e.g., plagioclase, pyroxene, and glass) have roughly overlapping absorption regions of approximately similar magnitude. Thus, despite the small crystal sizes that are present, which for basalts can be on the order of microns, nonlinear spectral mixing is minimal.

A second possible explanation for abundance discrepancies between techniques relates to missing end-members in the TIR spectral library [e.g., *Feely and Christensen*, 1999; *Michalski et al.*, 2006]. Missing mineral phases in the library, or compositionally different mineral phases in the library, may result in significant differences between the known and modeled abundances. For example, chlorite compositions can vary widely, but only three chlorite spectra were available for our library. Additionally, as previously mentioned, sericite, a fine-grained mica, is a missing member in our spectral library but represents a large volume percentage as indicated by petrologic examination and confirmed by high XRD abundances of mica. Although sericite is compositionally diverse, analytical techniques have demonstrated its close resemblance to a very fine grained muscovite [*Eberl et al.*, 1987]. Thus, the underestimation of mica in the TIR is likely partially due to the absence of a sericite spectral library member, in addition to the clay-sized particle transparency issue discussed above.

Third, differences in spectral contrast between library spectra and component phases within the mixture can affect derived abundances. Most library spectra used in this study were collected from sand-sized grains (~710–1000 μm) [*Christensen et al.*, 2000] which have deep spectral contrast compared to smaller grains. Thus, the modeled abundance coefficients for some phases in fine-grained mixtures may be smaller than they would be for coarse-grained mixtures of identical proportions. This issue might contribute to the underestimation of quartz and mica in the mudstones (Figures 5 and 7). Note that the clay spectra in our library were mostly acquired from pressed pellets [e.g., *Michalski et al.*, 2006; *Che and Glotch*, 2012], which are expected to exhibit similar spectral contrast to clay minerals in mudstones. This could contribute to the reason why clay abundances have much lower deviations from the known, compared to quartz and mica (Figures 5 and 7).

A fourth reason may be related to differences in crystal orientation between our samples and the library spectra. With the exception of clay minerals, most of our library spectra were acquired from loose particulates (Table 1), which should have random crystal orientations. However, grains within our sedimentary rock samples could have preferred orientations. Because the position and shape of spectral absorptions in the TIR vary with crystallographic axis of the mineral [e.g., *Christensen et al.*, 2000], spectra from mixtures with strongly preferred crystal orientations might not be well modeled with our library spectra.

All of these effects could lead to incorrect abundances as well as substitution of other phases by the model to fit absorptions caused by missing phases. For example, TIR spectral models identified amorphous silica phases (glass + silica) in all of the mudstones and two sandstones examined. However, XRD patterns did not indicate any X-ray amorphous material.

6. Conclusions

From our evaluation of laboratory thermal emission spectroscopy of sedimentary rocks, we conclude that linear unmixing of TIR spectra is an advantageous technique to employ for deriving accurate bulk rock mineral abundances. However, there are limitations in discerning abundances of minerals that comprise the very fine silt to clay grain size fraction (<30 μm). Primary detrital quartz and feldspar grains are readily identified with the correct phases and abundances that are modeled generally within 6–11 vol %. All other mineral phases suffer higher inaccuracies, but as a group, still remain within <15 vol % of values derived from point counts or QXRD These absolute differences and uncertainties fall within the accuracy associated with traditional point count techniques, comparing well with previous bulk rock TIR models, and correlate with XRD derived abundances.

Among the mineral phases that make up the mudstones and the more fine-grained matrix component of sandstones, clay minerals are generally modeled accurately to within 7.1 ± 5.8 vol %, but micas are underestimated by ~25 vol % or more. Conversely, amorphous silica and carbonate abundances are typically overestimated, with average overestimation of carbonates by ~6 vol % and silica by ~12.5 vol %.

The identification of mineral phases that contribute to the very fine silt to clay grain size fraction (<30 μm) remains ambiguous among the techniques examined, with each technique constrained by its intrinsic limitations. Traditional petrographic analysis of thin sections produces accurate estimates of mineral clasts as well as the percentage of matrix (or cement) present but can only qualitatively assess the content in the matrix fraction. Powdered X-ray diffraction requires extended sample preparation in order to identify discrete clay phases and (or) any poorly crystalline phases. Finally, TIR conventional linear least squares spectral models [e.g., *Ramsey and Christensen*, 1998; *Rogers and Aharonson*, 2008] are less effective on very fine-grained (< ~10 μm) material; however, this problem could be overcome with the use of other multivariate techniques, as described in paper 2. The investigation of the individual uncertainties associated with multiple techniques in determining bulk mineralogy demonstrates the utility that thermal emission spectroscopy can have in both terrestrial and planetary settings. Remote sensing using thermal emission spectroscopy has the ability to provide a rapid and passive analysis of sedimentary rocks and structures, with accuracies similar to the other techniques examined in this study. Such analysis could guide further sample investigations that use complementary geochemical and mineralogical techniques, such as X-ray fluorescence or diffraction. The overall ability of TIR to distinguish a mudstone from other clastic sedimentary rocks is comparable between techniques and therefore demonstrates the usefulness of this technique in assessing provenance, depositional, and diagenetic history of sedimentary materials.

Acknowledgments
We are grateful for discussions and comments provided by Scott McLennan, Timothy Glotch, and Steven Jaret. The authors would like to thank Scott McLennan, Troy Rasbury, and Kevin Cannon for donating the samples used for this investigation. We acknowledge funding from the NASA Mars Fundamental Research Program grant NNX09AL22G to A.D.R. We appreciate thorough and useful reviews from Mikki Osterloo and an anonymous reviewer. Sources for the library spectra used in this work are described in Table 1. All sandstone and mudstone spectra measured for this paper will be made available at http://aram.ess.stonybrook.edu/drogers/ upon acceptance of this manuscript.

References

Aronson, J. R., A. G. Emslie, R. V. Allen, and H. G. McLinden (1967), Studies of the middle- and far-infrared spectra of mineral surfaces for application in remote compositional mapping of the moon and planets, *J. Geophys. Res.*, *72*, 687–703, doi:10.1029/JZ072i002p00687.

Baldridge, A., J. Farmer, and J. Moersch (2004), Mars remote-sensing analog studies in the Badwater Basin, Death Valley, California, *J. Geophys. Res.*, *109*, E12006, doi:10.1029/2004JE002315.

Baldridge, A. M. (2008), Thermal emission studies of sulfates and chlorides: Implications for salts on the Martian surface, PhD dissertation, Arizona State Univ., Tempe.

Bandfield, J. (2008), High-silica deposits of an aqueous origin in western Hellas Basin, Mars, *Geophys. Res. Lett.*, *35*, LI2205, doi:10.1029/2008GL033807.

Bandfield, J., V. Hamilton, and P. Christensen (2000), A global view of Martian surface compositions from MGS-TES, *Science*, *287*(5458), 1626–1630, doi:10.1126/science.287.5458.1626.

Bandfield, J. L. (2002), Global mineral distributions on Mars, *J. Geophys. Res.*, *107*(E6), 5042, doi:10.1029/2001JE001510.

Bibring, J., et al. (2006), Global mineralogical and aqueous mars history derived from OMEGA/Mars express data, *Science*, *312*(5772), 400–404, doi:10.1126/science.1122659.

Blatt, H., R. J. Tracy, and B. E. Owens (2006), *Petrology Igneous, Sedimentary, and Metamorphic*, 3rd ed., W.H. Freeman and Company, New York.

Boggs, S., Jr. (1987), *Petrology of Sedimentary Rocks*, Macmillan, New York.

Cannon, K. M., J. F. Mustard, and M. R. Salvatore (2015), Alteration of immature sedimentary rocks on Earth and Mars: Recording aqueous and surface-atmosphere processes, *Earth Planet. Sci. Lett.*, *417*, 78–86.

Carter, J., F. Poulet, J. P. Bibring, and S. Murchie (2010), Detection of hydrated silicates in crustal outcrops in the northern plains of Mars, *Science*, *328*(5986), 1682–1686.

Che, C., and T. Glotch (2012), The effect of high temperatures on the mid-to-far-infrared emission and near-infrared reflectance spectra of phyllosilicates and natural zeolites: Implications for Martian exploration, *Icarus*, *218*(1), 585–601, doi:10.1016/j.icarus.2012.01.005.

Christensen, P., J. Bandfield, V. Hamilton, D. Howard, M. Lane, J. Piatek, S. Ruff, and W. Stefanov (2000), A thermal emission spectral library of rock-forming minerals, *J. Geophys. Res.*, *105*(E4), 9735–9739, doi:10.1029/1998JE000624.

Christensen, P., et al. (2001), Mars Global Surveyor Thermal Emission Spectrometer experiment: Investigation description and surface science results, *J. Geophys. Res.*, *106*(E10), 23,823–23,871, doi:10.1029/2000JE001370.

Christensen, P. R. (1998), Variations in Martian surface composition and cloud occurrence determined from thermal infrared spectroscopy: Analysis of Viking and Mariner 9 data, *J. Geophys. Res.*, *103*(E1), 1733–1746, doi:10.1029/97JE02114.

Dott, R. H., Jr. (1964), Wacke, Graywacke and Matrix – What approach to immature sandstone classification?, *J. Sediment. Petrol.*, *34*, 625–632.

Eberl, D. D. (2003), User guide to RockJock- A program for determining quantitative mineralogy from x-ray diffraction data, *U.S. Geol. Surv. Open File Rep. 03-78*, p. 48.

Eberl, D. D., V. C. Farmer, and R. M. Barrer (1984), Clay Mineral formation and transformation in rock and soils, *Philos. Trans. R. Soc. London*, *311*, 241–257.

Eberl, D. D., J. Środon, M. Lee, P. H. Nadeau, and H. R. Northrop (1987), Sericite from the Silverton caldera, Colorado: Correlation among structure, composition, origin, and particle thickness, *Am. Mineral.*, *72*, 914–934.

Ehlmann, B. L., et al. (2008), Clay minerals in delta deposits and organic preservation potential on Mars, *Nat. Geosci.*, *1*(6), 355–358.

Ehlmann, B. L., D. L. Bish, S. W. Ruff, and J. F. Mustard (2011a), Mineralogy and chemistry of altered Icelandic basalts: Application to clay mineral detection and understanding aqueous environments on Mars, *J. Geophys. Res.*, *117*, E00J16, doi:10.1029/2012JE004156.

Ehlmann, B. L., J. F. Mustard, S. L. Murchie, J. P. Bibring, A. Meunier, A. A. Fraeman, and Y. Langevin (2011b), Subsurface water and clay mineral formation during the early history of Mars, *Nature*, *479*(7371), 53–60.

Fassett, C. I., and J. W. Head (2005), Fluvial sedimentary deposits on Mars: Ancient deltas in a crater lake in the Nili Fossae region, *Geophys. Res. Lett.*, *32*, L14201, doi:10.1029/2005GL023456.

Fedo, C., G. Young, H. Nesbitt, and J. Hanchar (1997), Potassic and sodic metasomatism in the Southern Province of the Canadian Shield: Evidence from the Paleoproterozoic Serpent Formation, Huronian Supergroup, Canada, *Precambrian Res.*, *84*(1–2), 17–36, doi:10.1016/S0301-9268(96)00058-7.

Feely, K., and P. Christensen (1999), Quantitative compositional analysis using thermal emission spectroscopy: Application to igneous and metamorphic rocks, *J. Geophys. Res.*, *104*(E10), 24,195–24,210, doi:10.1029/1999JE001034.

Gendrin, A., et al. (2005), Sulfates in Martian layered terrains: The OMEGA/Mars Express view, *Science*, *307*(5715), 1587–1591.

Glotch, T., and P. Christensen (2005), Geologic and mineralogic mapping of Aram Chaos: Evidence for a water-rich history, *J. Geophys. Res.*, *110*, E09006, doi:10.1029/2004JE002389.

Glotch, T., and A. Rogers (2007), Evidence for aqueous deposition of hematite- and sulfate-rich light-toned layered deposits in Aureum and Iani Chaos, Mars, *J. Geophys. Res.*, *112*, E06001, doi:10.1029/2006JE002863.

Glotch, T., J. Bandfield, P. Christensen, W. Calvin, S. McLennan, B. Clark, A. Rogers, and S. Squyres (2006), Mineralogy of the light-toned outcrop at Meridiani Planum as seen by the Miniature Thermal Emission Spectrometer and implications for its formation, *J. Geophys. Res.*, *111*, E12S03, doi:10.1029/2005JE002672.

Glotch, T. D., R. V. Morris, P. R. Christensen, and T. G. Sharp (2004), Effects of precursor mineralogy on the thermal infrared emission spectra of hematite: Application to Martian hematite mineralization, *J. Geophys. Res.*, *109*, E07003, doi:10.1029/2003JE002224.

Grotzinger, J., et al. (2014), A habitable fluvio-lacustrine environment at Yellowknife Bay, Gale Crater, Mars, *Science*, *343*(6169), doi:10.1126/science.1242777.

Hamilton, V., and P. Christensen (2000), Determining the modal mineralogy of mafic and ultramafic igneous rocks using thermal emission spectroscopy, *J. Geophys. Res.*, *105*(E4), 9717–9733, doi:10.1029/1999JE001113.

Hamilton, V., P. Christensen, and H. McSween (1997), Determining the compositions of Martian meteorites using thermal infrared emission spectroscopy: A precursor to Martian surface spectroscopy, *Meteorit. Planet. Sci.*, *32*(4), A55–A55.

Hardgrove, C., and A. D. Rogers (2014), Natural micron-scale roughness of chemical sedimentary rocks and effects on thermal infrared spectra, *Eighth International Conference on Mars* [#1392].

Hecker, C., M. van der Meijde, and F. van der Meer (2010), Thermal infrared spectroscopy on feldspars - Successes, limitations and their implications for remote sensing, *Earth Sci. Rev.*, *103*(1–2), 60–70, doi:10.1016/j.earscirev.2010.07.005.

Howard, A. D., J. M. Moore, and R. P. Irwin (2005), An intense terminal epoch of widespread fluvial activity on early Mars: 1. Valley network incision and associated deposits, *J. Geophys. Res.*, *110*, E12S14, doi:10.1029/2005JE002459.

Hunt, G. R., and L. M. Logan (1972), Variation of single particle mid-infrared emission spectrum with particle size, *Appl. Opt.*, *11*(1), 142–147.

Irwin, R. P., R. A. Craddock, and A. D. Howard (2005), Interior channels in Martian valley networks: Discharge and runoff production, *Geology*, *33*(6), 489–492.
Kieffer, H. H., and A. P. Zent (1992), Quasi-periodic climatic change on Mars, in *Mars*, edited by H. H. Kieffer et al., pp. 1180–1218, Univ. of Arizona Press, Tucson.
Koeppen, W. C., and V. E. Hamilton (2008), Global distribution, compositions, and abundances of olivine on the surface of Mars from thermal infrared data, *J. Geophys. Res.*, *113*, E05001, doi:10.1029/2007JE002984.
Lawson, C. L., and R. J. Hanson (1974), *Solving Least Square Problems*, vol. 161, Prentice-hall, Englewood Cliffs, N. J.
Malin, M. C., and K. S. Edgett (2000), Sedimentary rocks of early Mars, *Science*, *290*(5498), 1927–1937, doi:10.1126/science.290.5498.1927.
Manger, G. E. (1963), Porosity and bulk density of sedimentary rocks, *U.S. Geol. Surv. Bull.*, 1144-E.
Mathew, G., A. Nair, T. Rao, and K. Pande (2009), Laboratory technique for quantitative thermal emissivity measurements of geological samples, *J. Earth Syst. Sci.*, *118*(4), 391–404.
McLennan, S., et al. (2014), Elemental geochemistry of sedimentary rocks at Yellowknife Bay, Gale Crater, Mars, *Science*, *343*(6169), doi:10.1126/science.1244734.
McLennan, S. M., B. Fryer, and G. Young (1979), Rare-earth elements in Huronian (lower proterozoic) sedimentary rocks: Composition and evolution of the post-kenoran upper crust, *Geochim. Cosmochim. Acta*, *43*(3), 375–388, doi:10.1016/0016-7037(79)90202-3.
McLennan, S. M., S. Hemming, D. K. McDaniel, and G. N. Hanson (1993), Geochemical approaches to sedimentation, provenance, and tectonics, *Geol. Soc. Am. Spec. Pap.*, *284*, 21–40.
McLennan, S. M., et al. (2005), Provenance and diagensis of the evaporite-bearing Burns formation, Meridiani Planum, Mars, *Earth Planet. Sci. Lett.*, *240*(1), 95–121.
Metz, J. M., J. P. Grotzinger, D. Mohrig, R. Milliken, B. Prather, C. Pirmez, A. S. McEwen, and C. M. Weitz (2009), Sublacustrine depositional fans in southwest Melas Chasma, *J. Geophys. Res.*, *114*, E10002, doi:10.1029/2009JE003365.
Michalski, J., M. Kraft, T. Diedrich, T. Sharp, and P. Christensen (2003), Thermal emission spectroscopy of the silica polymorphs and considerations for remote sensing of Mars, *Geophys. Res. Lett.*, *30*(19), 2008, doi:10.1029/2003GL018354.
Michalski, J., S. Reynolds, T. Sharp, and P. Christensen (2004), Thermal infrared analysis of weathered granitic rock compositions in the Sacaton Mountains, Arizona: Implications for petrologic classifications from thermal infrared remote-sensing data, *J. Geophys. Res.*, *109*, E03007, doi:10.1029/2003JE002197.
Michalski, J., M. Kraft, T. Sharp, L. Williams, and P. Christensen (2006), Emission spectroscopy of clay minerals and evidence for poorly crystalline aluminosilicates on Mars from Thermal Emission Spectrometer data, *J. Geophys. Res.*, *111*, E03004, doi:10.1029/2005JE002438.
Michalski, J. R., J. Cuadros, P. B. Niles, J. Parnell, A. D. Rogers, and S. P. Wright (2013), Groundwater activity on Mars and implications for a deep biosphere, *Nat. Geosci.*, *6*(2), 133–138.
Milliken, R. E., et. al. (2008), Opaline silica in young deposits on Mars, *Geology*, *36*(11), 847–850.
Moersch, J. E., and P. R. Christensen (1995), Thermal emission from particulate surfaces: A comparison of scattering models with measured spectra, *J. Geophys. Res.*, *100*(E4), 7465–7477.
Moore, J. M., A. D. Howard, W. E. Dietrich, and P. M. Schenk (2003), Martian layered fluvial deposits: Implications for Noachian climate scenarios, *Geophys. Res. Lett.*, *30*(24), 2292, doi:10.1029/2003GL019002.
Morris, R., et al. (2010), Identification of carbonate-rich outcrops on Mars by the Spirit Rover, *Science*, *329*(5990), 421–424, doi:10.1126/science.1189667.
Murchie, S., et al. (2009), Compact Reconnaissance Imaging Spectrometer for Mars investigation and data set from the Mars Reconnaissance Orbiter's primary science phase, *J. Geophys. Res.*, *114*, E00D07, doi:10.1029/2009JE003344.
Nesbitt, H. W., and G. M. Young (1982), Early Proterozoic climates and plate motions inferred from major element chemistry of lutites, *Nature*, *299*(5885), 715–717.
Osterloo, M. M., et al. (2008), Chloride-bearing materials in the southern highlands of Mars, *Science*, *319*(5870), 1651–1654.
Pan, C., A. D. Rogers, and M. T. Thorpe (2015), Quantitative compositional analysis of sedimentary materials using thermal emission spectroscopy: 2. Application to compacted fine-grained mineral mixtures and assessment of applicability of Partial Least Squares (PLS) methods, *J. Geophys. Res. Planets*, *120*, doi:10.1002/2015JE004881.
Ramsey, M., and P. Christensen (1998), Mineral abundance determination: Quantitative deconvolution of thermal emission spectra, *J. Geophys. Res.*, *103*(B1), 577–596, doi:10.1029/97JB02784.
Realmuto, V. (1990), Separating the effects of temperature and emissivity: Emissivity spectrum normalization, *Proc. of the Second TIMS Workshop*, JPL Publ., 90–55, pp. 26–30.
Rogers, A., and O. Aharonson (2008), Mineralogical composition of sands in Meridiani Planum determined from Mars Exploration Rover data and comparison to orbital measurements, *J. Geophys. Res.*, *113*, E06S14, doi:10.1029/2007JE002995.
Rogers, A. D., and P. R. Christensen (2007), Surface mineralogy of Martian low-albedo regions from MGS-TES data: Implications for upper crustal evolution and surface alteration, *J. Geophys. Res.*, *112*, E01003, doi:10.1029/2006JE002727.
Ruff, S., P. Christensen, P. Barbera, and D. Anderson (1997), Quantitative thermal emission spectroscopy of minerals: A laboratory technique for measurement and calibration, *J. Geophys. Res.*, *102*(B7), 14,899–14,913, doi:10.1029/97JB00593.
Ruff, S., P. Christensen, D. Blaney, W. Farrand, J. Johnson, J. Michalski, J. Moersch, S. Wright, and S. Squyres (2006), The rocks of Gusev Crater as viewed by the Mini-TES instrument, *J. Geophys. Res.*, *111*, E12S18, doi:10.1029/2006JE002747.
Ruff, S., P. Niles, F. Alfano, and A. Clarke (2014), Evidence for a Noachian-aged ephemeral lake in Gusev crater, Mars, *Geology*, *42*(4), 359–362, doi:10.1130/G35508.1.
Salisbury, J. W., and A. Wald (1992), The role of volume scattering in reducing spectral contrast of reststrahlen bands in spectra of powdered minerals, *Icarus*, *96*(1), 121–128.
Sharma, S. R. (2015), *Thermo-Physical Properties of Rocks: Special Reference to Deccan Trap Basalts*, 180 pp., Allied Publishers, New Delhi.
Squyres, S., et al. (2004), In situ evidence for an ancient aqueous environment at Meridiani Planum, Mars, *Science*, *306*(5702), 1709–1714, doi:10.1126/science.1104559.
Squyres, S., et al. (2006), Rocks of the Columbia Hills, *J. Geophys. Res.*, *111*, E02S11, doi:10.1029/2005JE002562.
Środon, J., V. Drits, D. McCarty, J. Hsieh, and D. Eberl (2001), Quantitative X-ray diffraction analysis of clay-bearing rocks from random preparations, *Clays Clay Miner.*, *49*(6), 514–528, doi:10.1346/CCMN.2001.0490604.
Taylor, S. R., et al. (1981), The composition and evolution of the continental crust: Rare earth element evidence from sedimentary rocks, *Philos. Trans. R. Soc. London*, *301*, 381–299.
Thomson, J., and J. Salisbury (1993), The midinfrared reflectance of mineral mixtures (7–14 μm), *Remote Sens. Environ.*, *45*(1), 1–13, doi:10.1016/0034-4257(93)90077-B.
Van der Plas, D., and A. C. Tobi (1965), A chart for judging reliability of point counting results, *Am. J. Sci.*, *264*(1), 87–90.

Vaniman, D., et al. (2014), Mineralogy of a mudstone at Yellowknife Bay, Gale Crater, Mars, *Science*, *343*(6169), doi:10.1126/science.1243480.
Vincent, R. K., and G. R. Hunt (1968), Infrared reflectance from mats surfaces, *Appl. Opt.*, *7*(1), 53–59.
Weltje, G., and H. von Eynatten (2004), Quantitative provenance analysis of sediments: Review and outlook, *Sediment. Geol.*, *171*(1–4), 1–11, doi:10.1016/j.sedgeo.2004.05.007.
Williams, C. S. (1961), Discussion of the theories of cavity-type sources of radiant energy, *J. Opt. Soc. Am.*, *51*, 564–571.
Williams, H., F. J. Turner, and C. G. Gilbert (1954), *Petrography: An Introduction to the Study of Rock in Thin Sections*, W.H. Freeman and Company, San Francisco.
Wood, W. W., and L. A. Fernandez (1988), Volcanic rocks, chap. 39, in *Hydrogeology, The Geology of North America*, vol. 0–2, edited by W. Back, J. S. Rosenshein, and P. R. Seaber, pp. 353–365, Geol. Soc. Am., Decade of North American Geol. Project, Boulder, Colo.
Wray, J. J., S. L. Murchie, S. W. Squyres, F. P. Seelos, and L. L. Tornabene (2009), Diverse aqueous environments on ancient Mars revealed in the southern highlands, *Geology*, *37*(11), 1043–1046.
Wyatt, M., V. Hamilton, H. McSween, P. Christensen, and L. Taylor (2001), Analysis of terrestrial and Martian volcanic compositions using thermal emission spectroscopy: 1. Determination of mineralogy, chemistry, and classification strategies, *J. Geophys. Res.*, *106*(E7), 14,711–14,732, doi:10.1029/2000JE001356.